The TWK-26/KCNK3 potassium channel and FLR-4 protein kinase coordinate nutrient absorption in the *C. elegans* intestine

Sarah K. Torzone[1], Trae Carroll[2], Peter C. Breen[1], Natalie R. Cohen[1], Kaylee N. Simmons[1], Kylie R. VanDerMolen[3], Keith W. Nehrke[4], Robert H. Dowen[1,5,6*]

[1]Integrative Program for Biological and Genome Sciences, The University of North Carolina at Chapel Hill, Chapel Hill, North Carolina, United States of America

[2]Department of Pathology, University of Rochester Medical Center, Rochester, New York, United States of America

[3]Curriculum in Genetics and Molecular Biology, The University of North Carolina at Chapel Hill, Chapel Hill, North Carolina, United States of America

[4]Department of Medicine, Nephrology Division, University of Rochester Medical Center, Rochester, New York, United States of America

[5]Department of Biology, The University of North Carolina at Chapel Hill, Chapel Hill, North Carolina, United States of America

[6]Department of Cell Biology and Physiology, The University of North Carolina at Chapel Hill, Chapel Hill, North Carolina, United States of America

* Corresponding author

E-mail: dowen@email.unc.edu

ABSTRACT

Ion channels are necessary for proper water and nutrient absorption in the intestine, thereby supporting cellular metabolism and organismal growth. While a role for Na^+ co-transporters and pumps in intestinal nutrient absorption is well defined, how individual K^+ uniporters function in this process is poorly understood. Using *Caenorhabditis elegans*, we show that a gain-of-function mutation in *twk-26*, which encodes a two-pore domain K^+ ion channel orthologous to human KCNK3, facilitates nutrient absorption and suppresses the metabolic and developmental defects caused by loss of DRL-1/FLR-4 signaling. Mutations in *drl-1* and *flr-4,* which encode two unique kinases that are components of a mitogen-activated protein kinase (MAPK) pathway, and the downstream *flr-1* Na^+ ion channel, cause severe growth defects, reduced lipid storage, and a dramatic increase in autophagic lysosomes, which mirror dietary restriction phenotypes. We reveal that this dietary restriction phenotype is likely the result of impaired intestinal amino acid absorption, which is restored upon activation of TWK-26. Furthermore, we show that loss of *flr-4* disrupts intracellular and extracellular pH gradients, suggesting that the FLR-4 pathway may be necessary to maintain intestinal ion homeostasis and facilitate nutrient absorption. The altered pH gradients in the *flr-4* mutant are partially restored by activation of TWK-26, demonstrating a novel role for this K^+ ion channel in governing intestinal physiology and metabolism.

42 **INTRODUCTION**

43 Ion channels are membrane proteins that regulate the excitability of specialized cells that generate
44 and propagate action potentials, as well as cell types that generate ion gradients to govern water,
45 electrolyte, and small molecule transport across membranes. In the intestine, the maintenance of
46 membrane potential and transmembrane ion gradients is essential for nutrient absorption and digestion
47 (Lu et al. 2023). Dysregulation of ion channel expression or function in intestinal enterocytes contributes
48 to several gastrointestinal (GI) pathologies, as seen in cystic fibrosis, colonic inflammation, and colorectal
49 cancers (Anderson et al. 2019). For example, intermediate conductance potassium ion (IK) channels on
50 the basolateral membrane of colonocytes are required for membrane hyperpolarization that facilitate Na^+
51 and Cl^- transport across the cell membrane, which when impaired results in diseases such as ulcerative
52 colitis (Al-Hazza et al. 2012). Consistently, decreased expression of basolateral IK channels in
53 inflammatory bowel disease results in the secretion of K^+ ions into the intestinal lumen, causing
54 abdominal pain and diarrhea (Magalhães et al. 2016). Because ion channels are essential for preserving
55 gastrointestinal function and organismal energy homeostasis, it is crucial to understand the molecular
56 mechanisms that govern their activity in order to identify novel therapeutic targets of GI disease.

57 The depolarization or hyperpolarization of intestinal epithelial cells (IECs) is largely responsible
58 for tuning the activity of nutrient transporters (Lu et al. 2023). For example, the transport of peptides by
59 the di/tripeptide nutrient transporter PepT1 requires the recycling of an H^+ ion gradient across the apical
60 membrane of IECs (Thwaites et al. 2002). Thus, proper nutrient absorption in the intestine is pH
61 dependent. The electrogenic forces that drive proton-coupled amino acid and glucose absorption in IECs
62 are often stabilized by K^+ channels (Lu et al. 2023), but how specific potassium ion channels regulate
63 metabolic processes in the intestine to promote organismal homeostasis remains poorly understood.

64 Regulation of intestinal nutrient absorption by ion gradients is well conserved. In the nematode
65 *Caenorhabditis elegans*, 20 epithelial cells absorb all the lipids, peptides, and carbohydrates required to
66 maintain metabolic homeostasis and promote growth. The *C. elegans* gene *pept-1* encodes an intestinal

67 oligopeptide transporter that is the ortholog of mammalian PepT1. As the primary di/tri-peptide
68 transporter in the intestine, loss of *pept-1* impairs amino acid uptake, which slows development and
69 reduces body size in *C. elegans* (Nehrke 2003). Likewise, loss of the apical Na^+/H^+ exchanger NHX-
70 2/NHE3, an intestinal antiporter that maintains intestinal acidification and drives pH-dependent nutrient
71 absorption, impairs growth and development (Nehrke 2003). Furthermore, disruption of *nhx-2* blunts lipid
72 absorption, possibly arising from PEPT-1-dependent intracellular acidification (Spanier et al. 2009).
73 Intestinal pH oscillations, which support nutrient absorption and metabolic homeostasis, are also
74 necessary to promote a rhythmic defecation cycle in *C. elegans*. The *C. elegans* defecation motor program
75 (DMP) occurs every ~45 seconds and is coordinated by calcium and proton oscillations in the intestine
76 (Iwasaki et al. 1995; Branicky and Hekimi 2006; Allman et al. 2009; Pfeiffer et al. 2008). The DMP is
77 coupled to the absorption of essential nutrients, including dipeptides, glucose, and lipids (Allman et al.
78 2009; Sheng et al. 2015; Suzuki et al. 2022). Consistently, mutations that disrupt the DMP (*e.g.*, *aex-5* and
79 *flr-1*) reduce somatic intracellular lipid stores (Kaulich et al. 2022; Sheng et al. 2015), likely due to
80 impaired intestinal acidification and poor nutrient absorption. It is known that cell autonomous calcium
81 signaling drives the ultradian DMP, and the mechanisms that regulate intestinal calcium oscillations are
82 well defined (Estevez and Strange 2005). Thus, maintenance of intestinal ion homeostasis is imperative to
83 the metabolic homeostasis of the organism, governing both defecation and nutrient absorption; however,
84 the molecular mechanisms that connect these ion-driven processes has remained elusive.
85 We previously demonstrated that DRL-1 and FLR-4, two intestinal protein kinases that function
86 upstream of a mitogen-activated protein kinase (MAPK) signaling pathway, promote growth, lipid
87 accumulation, and reproduction in *C. elegans* by, at least in part, suppressing the p38 innate immune
88 pathway (Torzone et al. 2023). Loss-of-function alleles of *drl-1* (also known as *flr-3*) (Honey et al. 2023),
89 *flr-4*, and *flr-1* were isolated in a forward genetic screen for mutations that confer resistance to fluoride
90 (Katsura et al. 1994). The *flr-1* gene encodes a degenerin (DEG)/epithelial sodium channel (ENaC).
91 Intriguingly, mutations in *drl-1*, *flr-4*, and *flr-1* all disrupt the DMP, cause developmental delay, and

92 reduce lipid stores (Chamoli et al. 2014; Katsura et al. 1994; Kaulich et al. 2022; Take-uchi et al. 1998,
93 2005; Torzone et al. 2023), suggesting that DRL-1/FLR-4 signaling and ion channels may function in
94 concert to coordinate defecation, metabolism, and development; however, the mechanistic basis of this
95 regulation is unknown.

96 In this study, we use a forward genetic approach to isolate a gain-of-function mutation in *twk-26*,
97 which encodes a potassium two-pore domain (K2P) ion channel, that suppresses the metabolic and
98 developmental defects conferred by the *flr-4* and *flr-1* mutations. Additionally, we establish that an
99 activating mutation that increases the open probability of TWK-26 mimics the gain-of-function *twk-26*
100 mutation, suggesting that the role of TWK-26 in metabolic homeostasis is linked to its ion channel
101 activity. Remarkably, we find that loss of *flr-4* and *flr-1* severely impairs intestinal dipeptide absorption
102 and the intestinal pH gradients that are essential for this process, both of which are restored when TWK-
103 26 is activated. Additionally, we show that the *twk-26* gain-of-function mutation fails to suppress the
104 defects in the defecation motor program displayed by *flr-4* and *flr-1* mutants, demonstrating that nutrient
105 absorption can be uncoupled from the DMP. Our study provides new mechanistic insight into the dual
106 regulation of intestinal metabolism by K^+ ion homeostasis and protein kinase signaling.
107

108 **RESULTS**

109 **A mutation in the TWK-26 potassium channel reverses the metabolic defects conferred by impaired**
110 **FLR-4 signaling**

111 In *C. elegans*, the intestinal protein kinase FLR-4 promotes growth and maintains lipid
112 homeostasis, partially through regulation of the p38 MAPK pathway (Torzone et al. 2023). Additionally,
113 *flr-4* is required for maximal expression of the intestinal vitellogenin proteins (VIT-1-6), which mediate
114 the transport of lipids to mature oocytes via lipoprotein particles thereby supporting reproduction and
115 embryonic development (Kimble and Sharrock 1983; Torzone et al. 2023). Consistently, loss of *flr-4*, or

116 its kinase activity, results in a striking reduction in body size, growth rate, and intestinal vitellogenin
117 expression.

118 The downstream targets of FLR-4, which may be other kinases that act in a canonical signaling
119 cascade, are unknown. Expression of the P*vit-3::GFP* vitellogenesis reporter, which consists of the *vit-3*
120 promoter driving GFP (Dowen et al. 2016), is markedly down-regulated after loss of *flr-4*. While adult-
121 specific expression of the vitellogenin proteins is under strict developmental control, their transcriptional
122 regulation is also tied to nutrient sensing mechanisms, as reduced caloric intake decreases the rate of
123 vitellogenin production (Seah et al. 2016; Perez and Lehner 2019). We sought to identify additional
124 components of the FLR-4 pathway and to define whether FLR-4 acts via developmental or nutritional
125 mechanisms to regulate vitellogenesis. To that end, we conducted a forward genetic screen for mutations
126 that suppress the P*vit-3::GFP* expression defects in the *flr-4(ut7)* mutant (Figure 1A). We specifically
127 targeted suppressors in the F1 generation to enrich for gain-of-function suppressor mutations. Following
128 backcrossing to the non-mutagenized strain, we performed whole genome sequencing of the suppressor
129 mutants and identified candidate causative mutations using computational approaches. Remarkably, we
130 identified four, independently generated, instances of the same mutation in *twk-26*, which encodes a two-
131 pore domain potassium (K2P) ion channel (Figure 1A). The *C. elegans* genome encodes 47 K2P channels,
132 most of which have unknown functions (Hobert 2013), including *twk-26*. K2P channels are a class of
133 potassium leak channels that possess four transmembrane domains and two pore-forming domains
134 (Feliciangeli et al. 2015). The TOPCONS protein topology prediction (Tsirigos et al. 2015) for TWK-26
135 identified four transmembrane domains (Figure 1B), which is consistent with the structure of other K2P
136 channels. The EMS-generated mutation in TWK-26, G485E, is positioned within the C- terminus. The
137 role of TWK-26 in metabolic homeostasis is surprising, as potassium ion leak channels are known to play
138 a role in neurotransmission and vascular tone modulation in mammals, but little is known about
139 potassium channels outside of these excitable tissues (Feliciangeli et al. 2015).

140 We previously demonstrated that loss of GPLA-1, a neuronally-expressed glycoprotein hormone
141 also known as FLR-2, its receptor, FSHR-1, or downstream cAMP signaling suppressed the growth and
142 metabolic defects displayed by the *flr-4* mutant (Torzone et al. 2023). Using the highly sensitive single-
143 copy P*vit-3::mCherry* transcriptional reporter (Cully et al. 2024), we confirmed that the *twk-26(G485E)*
144 mutation partially suppressed the vitellogenesis defects conferred by the *flr-4* mutation, but not to the
145 same extent as the *gpla-1* mutation (Figure 1C-D). To further elucidate the role of TWK-26 in growth and
146 metabolic homeostasis, we compared the development of the *flr-4(ut7)* single mutant to the *flr-4(ut7) twk-*
147 *26(G485E)* double mutant. Interestingly, the *twk-26(G485E)* allele strongly suppressed the developmental
148 delay and body size defects conferred by the *flr-4* mutation to levels similar to that of the *gpla-1* allele
149 (Figure 1E-F). Somatic lipid accumulation, as determined by Oil Red O and Nile Red staining, was also
150 partially suppressed by the *twk-26* mutation (Figures 1G-H). Together, these results reveal that TWK-26
151 plays an important role in regulating growth and lipid homeostasis in conjunction with FLR-4.
152 The *flr-4(ut7)* allele, as well as mutations in *flr-1* and *flr-3*/*drl-1*, were isolated in a forward genetic
153 screen for mutations that confer resistance to fluoride (Katsura et al. 1994). FLR-1, an acid-sensing
154 sodium ion channel, and FLR-4 are known to colocalize and function together in the intestine (Kobayashi
155 et al. 2011). Furthermore, DRL-1 and FLR-4 form a protein kinase complex in the intestine (Torzone et al.
156 2023). Thus, we reasoned that if *twk-26(G485E)* suppressed the *flr-4(ut7)* mutation, it may also suppress
157 the *flr-1* and *drl-1* mutations. Indeed, the *twk-26* allele strongly suppressed the growth rate defects of the
158 *flr-1* and *drl-1* mutants, as well as provided a modest suppression of the P*vit-3::mCherry* expression
159 defects (Figure S1A-B). Additionally, the *twk-26(G485E)* mutation suppressed the lipid storage and body
160 size defects of the *flr-1* mutant to similar levels as the *gpla-1* mutation (Figure S1C-D), suggesting that
161 the metabolic and growth defects associated with loss of FLR-1 is due to impaired ion homeostasis.
162 Together, our data indicate that the TWK-26 potassium channel functions in concert with the FLR-4
163 signaling pathway to coordinate growth and lipid homeostasis in *C. elegans*.
164

165 **The *twk-26(G485E)* mutation is a gain-of-function allele**

166 We isolated the *twk-26(G485E)* allele in the F1 generation of an EMS mutagenesis screen,
167 suggesting that the G485E mutation confers either a gain-in-function or haploinsufficiency. To
168 differentiate between these two possibilities, we knocked-down *twk-26* using RNAi in the *flr-4(ut7)* and
169 *flr-4(ut7) twk-26(G485E)* mutants and assessed the resulting phenotypes. If *twk-26(G485E)* is
170 haploinsufficient, *twk-26* RNAi would suppress the growth rate, body size, and metabolic defects of the
171 *flr-4(ut7)* mutant; however, if *twk-26(G485E)* is a gain-of-function allele, *twk-26* RNAi would reverse the
172 suppressive effects that we observed in *flr-4(ut7) twk-26(G485E)* animals. Knock-down of *twk-26*
173 abrogated the suppressive effects of the *twk-26(G485E)* allele, producing animals with reduced
174 developmental rates and small body sizes that are characteristic of the *flr-4* mutant (Figure 2A-C).
175 Although *twk-26* RNAi yielded only a modest effect on P*vit-3::mCherry* expression in *flr-4(ut7) twk-*
176 *26(G485E)* animals, the *twk-26(G485E)* mutation alone significantly reduced the expression of the
177 vitellogenin reporter, which was reversed by *twk-26* RNAi (Figure S2A). Next, we generated a presumed
178 loss-of-function frameshift mutation within the *twk-26* locus by CRISPR/Cas9 editing and found that this
179 mutation failed to suppress the vitellogenesis defects and small body size of animals depleted for
180 intestinal FLR-4 (Figures S2B and S2C). Together, these data indicate that the *twk-26(G485E)* mutation is
181 a gain-of-function allele, providing unique molecular insight into our understanding of the TWK-26 K2P
182 channel. Thus, we presume that activation, and not inhibition, of the TWK-26 ion channel reverses the
183 dramatic developmental and metabolic defects of the *flr-4* mutant.

184 We next sought to identify the tissue where TWK-26 functions. It is mostly likely that TWK-26
185 functions cell-autonomously in the intestine, where FLR-4, FLR-1, and DRL-1 act to promote growth and
186 maintain lipid homeostasis (Kobayashi et al. 2011; Torzone et al. 2023). However, it is possible that
187 TWK-26 functions in neurons, where K2P channels have well-described roles in neurotransmission,
188 locomotion, and innervation of enteric muscles (Gottschling et al. 2017; Yue et al. 2022; Zhou et al.
189 2022). To define the tissues that express TWK-26, we first generated a P*twk-26::mCherry* transcriptional

190 reporter, which consists of ~1 kb of the *twk-26* promoter driving mCherry, and overexpressed the
191 transgene in animals as an extrachromosomal array. Surprisingly, we observed mCherry signal
192 specifically in the posterior intestine (Figure 2D), suggesting that *twk-26* expression is repressed in the
193 anterior intestine. To eliminate the possibility of overexpression and transgene artifacts, we used
194 CRISPR/Cas9 editing to insert a SL2::H2B::GFP cassette into the 3' end of the *twk-26* locus, which
195 generates a polycistronic pre-mRNA that is trans-spliced to generate both the *twk-26* and *h2b::gfp*
196 transcripts. Consistent with our previous results, we observed H2B::GFP expression specifically in the
197 posterior intestine (Figure 2E); however, *twk-26* may also be expressed in a small set of head neurons. To
198 establish whether *twk-26(G485E)* is required in either of these tissues to exert its suppressive effects, we
199 engineered a C-terminal auxin-inducible degron (AID) into the endogenous *twk-26(G485E)* locus by
200 CRISPR/Cas9 editing and performed pan-neuronal or intestine-specific depletion of TWK-26 using auxin.
201 Depletion of TWK-26 G485E in the intestine, but not in neurons, resulted in a decrease in body size and
202 lipid levels in animals lacking *flr-4* or *flr-1* (Figures 2F-G). Together, these data suggest that activation of
203 TWK-26 in the intestine, but not in neurons, restores proper growth and metabolic function upon loss of
204 FLR-4.
205

206 **Destabilized gating of the TWK-26 channel restores metabolic homeostasis following loss of *flr-4* or**
207 ***flr-1***

208 The predicted human ortholog of TWK-26 is KCNK3/TASK, a two-pore domain K^+ leak channel
209 that is broadly expressed, including in the brain and small intestine, and that is strongly inhibited by
210 extracellular acidification (Duprat et al. 1997). KCNK3 contains a structural motif called the X-gate,
211 which regulates the opening and closing of the channel (Rödström et al. 2020). We hypothesized that the
212 G485E gain-of-function mutation might confer increased ion conductance of the TWK-26 channel.
213 Therefore, we explored the possibility that mutations at positions conserved across K2P family members
214 that are known to increase conductance may also impact TWK-26 activity and suppress the *flr-4* mutant

215 defects. A previous study demonstrated that a leucine to asparagine substitution in the second
216 transmembrane domain of several *C. elegans* K2Ps increases channel activity and open probability (Ben
217 Soussia et al. 2019), suggesting that this residue is critical for gating of all K2P channels. Therefore, we
218 engineered the analogous mutation, L229N, into the *twk-26* locus using CRISPR/Cas9 genome editing
219 (Figure 3A). We predicted that if the G485E mutation increases ion conductance of the TWK-26 channel
220 to suppress the metabolic defects of the *flr-4* mutant, then the L229N mutation should confer the same
221 suppressor phenotype. Indeed, the *twk-26(L229N)* mutation suppressed the small body size and lipid
222 storage defects of *flr-4* or *flr-1* knock-down animals to a level similar to that of the *twk-26(G485E)*
223 mutation (Figures 3B-C). This result suggests that the *twk-26(G485E)* mutation identified in our EMS
224 screen confers a gain-in-function that increases conductance through the ion channel. Notably, the L229N
225 mutation was not recovered in our mutagenesis screen; however, the nucleotide conversions preferentially
226 generated by EMS mutagenesis would not be expected to generate this specific amino acid substitution.
227 Given that the G485E mutation is positioned in the C-terminus of TWK-26, we explored the
228 possibility that the C-terminus of the protein facilitates the increase in TWK-26 G485E activity. Using
229 CRISPR/Cas9 genome editing, we generated a strain expressing the TWK-26 G485E protein lacking the
230 wild-type C-terminus (*i.e.*, ΔSer503-Glu519, frameshift at Thr502). Indeed, the C-terminus of TWK-26 is
231 required for the gain-in-function, as the *twk-26(G485E, ΔCT)* mutation failed to suppress the small body
232 size of *flr-4* or *flr-1* knock-down animals (Figure 3D). These results argue that the C-terminus promotes
233 the gain-of-function activity of TWK-26 G485E; however, we cannot rule out the possibility that this
234 complex mutation impaired the normal function of TWK-26 altogether.
235
236 **TWK-26 G485E suppresses autophagy in dietary restriction-like mutants**
237 During dietary restriction (DR), organisms rewire metabolic pathways to initiate catabolic
238 programs, granting access to stored energy reserves when external nutrients are scarce. For example, rapid
239 depletion of intestinal lipids during the initial stages of starvation is a survival mechanism that is

240 conserved across species (Tan et al. 2011). In *C. elegans*, the transcription factor HLH-30, which is
241 orthologous to mammalian TFEB (Lapierre et al. 2013), up-regulates metabolic genes involved in
242 lipolysis during nutrient deprivation (O'Rourke and Ruvkun 2013). Importantly, HLH-30 couples the
243 breakdown of lipid droplet fats with autophagy (O'Rourke and Ruvkun 2013), which shuttles fats from
244 lipid droplets to lysosomes during lipophagy (Singh et al. 2009).

245 Reduced FLR-4, DRL-1, or FLR-1 signaling strongly induces a DR-like phenotype that is
246 characterized by loss of somatic lipid stores. Therefore, we hypothesized that the *flr-4* and *flr-1* mutants
247 would display an enhanced autophagic response that would be suppressed by activation of TWK-26. To
248 test this hypothesis, we used a dual-fluorescent mCherry::GFP::LGG-1 reporter to visualize the induction
249 of autophagy in *twk-26(G485E)* mutants. The mCherry::GFP::LGG-1 protein, which is orthologous to
250 Atg8, co-labels autophagosomes with mCherry/GFP and labels autolysosomes with only mCherry due to
251 pH quenching of the GFP (Chang et al. 2017). Because an increase in autophagic activity is accompanied
252 by an upregulation of autophagic vesicles (Chang et al. 2017), we quantified the number and size of
253 mCherry-labelled autolysosomes in intestinal cells to assess autophagic flux. We did not observe an
254 appreciable number of mCherry/GFP co-labeled puncta, consistent with a previous study that employed
255 this strain (Chang et al. 2017), and therefore, we did not quantify the number of autophagosomes.
256 Importantly, quantification of autolysosomes alone is a sufficient measure of autophagic activity, given
257 that the mCherry autolysosomes are known to co-localize with LysoTracker (Chang et al. 2017). We
258 found that knock-down of *flr-4* or *flr-1* by RNAi resulted in a dramatic increase in the amount and size of
259 intestinal autolysosomes (Figures 4A-B), indicating that autophagic activity was up-regulated in these
260 DR-like mutants. Crucially, this increase in autophagy was suppressed by *twk-26(G485E)*, suggesting that
261 activation of the TWK-26 channel suppresses the *flr*-induced DR-like response.

262 Given that loss of *flr-4* and *flr-1* increased autophagic flux, we hypothesized that the HLH-
263 30/TFEB transcription factor, which up-regulates autophagy factors during starvation (Settembre et al.
264 2013), would accumulate in the intestinal nuclei of the *flr* mutants. Surprisingly, knock-down of *flr-4* or

265 *flr-1* by RNAi severely reduced the levels of nuclear HLH-30 (Figures 4C-D), which was suppressed by
266 *twk-26(G485E)*. Consistently, knock-down of *hlh-30* by RNAi had little impact on P*vit-3::mCherry*
267 reporter expression nor the body sizes of the *flr-4* or *flr-4(ut7) twk-26(G485E)* mutants (Figures S3A-B).
268 We also observed that *twk-26(G485E)* alone promoted HLH-30 nuclear localization (Figures 4C-D),
269 suggesting that the animal may activate protective signaling to maximize resources under increased K^+
270 channel activity. These results argue that loss of *flr-4* or *flr-1* prompt an HLH-30-independent induction of
271 autophagy or that HLH-30 nuclear localization activates different pathways in different models of dietary
272 restriction.

273 Therefore, we investigated whether the starvation-responsive transcription factor HLH-11/TFAP4
274 responds to loss of *flr-4* or *flr-1*. HLH-11 represses the expression of lipid catabolism genes under well-
275 fed conditions and is degraded during starvation to release fat reserves for energy (Li et al. 2020). Indeed,
276 knock-down of *flr-4* or *flr-1* by RNAi reduced levels of nuclear HLH-11 in the intestine; however, this
277 reduction in HLH-11 nuclear signal was suppressed by the *twk-26(G485E)* allele (Figures 4E-F),
278 suggesting that TWK-26 activation prevents the degradation of HLH-11 when nutrients are available.
279 Together, these data argue that loss of FLR-4 signaling triggers an HLH-11-dependent, and HLH-30-
280 independent, induction of autophagy during dietary restriction. Thus, these data reveal a novel role for the
281 TWK-26 K2P channel in cellular metabolism, as activation of this ion channel partially reverses an
282 autophagic starvation response.

283

284 **The TWK-26 G485E mutation uncouples defecation cycle from lipid metabolism**

285 To understand how TWK-26 hyperactivation may be influencing intestinal metabolism to rectify
286 the lipid storage and developmental defects of the *flr* mutants, we first investigated whether the defecation
287 motor program (DMP) is altered in the *twk-26(G485E)* mutant. The *flr-4* and *flr-1* mutants display an
288 irregular defecation cycle (Iwasaki et al. 1995; Katsura et al. 1994; Take-uchi et al. 1998, 2005), resulting
289 in a 'constipated' phenotype that may contribute to their DR-like state (Take-uchi et al. 1998). This

290 phenotype, which likely results from improper expulsion of gut contents (Liu and Thomas 1994),
291 coincides with intestinal bloating (Gruss and Corsi 2022; Lin-Moore et al. 2021). Intestine bloating can be
292 indicative of increased microbial colonization, activation of innate immunity pathways, and initiation of
293 pathogen aversion behaviors (Singh and Aballay 2019). Consistently, an impaired DMP is associated with
294 intestinal bloating, enhanced susceptibility to pathogens, and DR-like phenotypes (Das et al. 2023), which
295 could underlie the metabolic and growth defects displayed by the *flr* mutants.

296 Therefore, we hypothesized that the *flr-4* and *flr*-1 mutants would show intestinal bloating and
297 increased immune signaling resulting from an irregular DMP, which would be suppressed by the *twk-*
298 *26(G485E)* mutation. We first examined the morphology of the intestinal lumen of animals expressing
299 ERM-1::eGFP, which localizes to the intestinal apical membrane and facilitates lumen width
300 measurements (Ramalho et al. 2020). Consistent with the previously reported DMP defects (Take-uchi et
301 al. 1998, 2005), knock-down of *flr-4* or *flr-1* by RNAi increased intestinal lumen width; however, the
302 bloating was not suppressed by the *twk-26(G485E)* mutation (Figures 5A-B). This result is surprising
303 since intestinal bloating is often associated with a DR-like state (Das et al. 2023), which is displayed by
304 the *flr* mutants and is suppressed by the *twk-26(G485E)* allele (Figures 1G-H and S1D). Furthermore,
305 activation of the p38 innate immune pathway, as assessed by oligomerization of the upstream p38
306 regulator TIR-1/SARM1 (Peterson et al. 2022), was stimulated by loss of *flr-4* as expected (Torzone et al.
307 2023); however, TIR-1 aggregation was not suppressed by the *twk-26(G485E)* allele (Figures 5C and
308 S4A-C). We also explored the possibility that the intestinal lumen bloating observed upon loss of *flr-4* or
309 *flr-1* could result from impaired feeding as previously observed in the *phm-2* and *eat-2* mutants, which
310 display food avoidance behaviors and dietary restriction phenotypes that are characteristic of intestinal
311 bloating (Kumar et al. 2019). Using pharyngeal pumping rates to assess feeding behavior (Avery 1993),
312 we found that the *flr-4* and *flr-1* mutants do not display severe feeding defects (Figure S5), as has been
313 observed for the *eat-2* mutant (Raizen et al. 1995; Lakowski and Hekimi 1998). Together, these data
314 reveal that the DR-like state of the *flr-4* and *flr-1* mutants is uncoupled from the intestinal bloating and

315 immunity phenotypes, suggesting that FLR-4 and FLR-1 may influence defecation, and ultimately
316 metabolic homeostasis, more directly.

317 The *C. elegans* DMP is a highly coordinated behavior that is temporally regulated, with a new
318 cycle initiated every 45 seconds and consisting of 3 steps, which together last for 5 seconds (Thomas
319 1990). These steps include a posterior body wall contraction (pBoc), an anterior body wall contraction
320 (aBoc), and an expulsion, which ultimately results in the release of gut contents. These contractions are
321 reliant on calcium oscillations (Dal Santo et al. 1999; Espelt et al. 2005), which are partially controlled by
322 FLR-1 (Kaulich et al. 2022). Many of the factors that regulate the DMP have been studied in detail;
323 however, it is not clear why *flr-4* and *flr-1* mutations shorten the DMP cycle and cause expulsion defects
324 (Branicky and Hekimi 2006; Iwasaki et al. 1995).

325 Because defecation is an ion-dependent process, we next explored whether the *twk-26(G485E)*
326 mutation, which likely increases K+ conductance, suppresses the irregularity of the DMP caused by the *flr*
327 mutations by altering intestinal ion flux. The DMP is known to promote absorption of glucose in the
328 intestine (Suzuki et al. 2022), and mutations in key DMP genes, like *flr-1*, restrict fat accumulation
329 (Kaulich et al. 2022). Therefore, it is possible that since the *twk-26(G485E)* allele suppressed the
330 metabolic phenotypes of the *flr-4* and *flr-1* mutants, it may also suppress the irregular defecation rhythm
331 of these animals to indirectly restore fat levels. Surprisingly, we found that *twk-26(G485E)* did not
332 suppress the short DMP interval nor increase the number of intestinal expulsion events in the *flr* mutants
333 (Figures 5D-E). Consistently, knock-down of *nlp-40*, which encodes an intestinal neuropeptide-like
334 protein that controls DVB neuron activity and the expulsion step of the DMP (Wang et al. 2013), resulted
335 in loss of P*vit-3::mCherry* reporter expression and reduced body size; however, these phenotypes were
336 not suppressed by the *twk-26(G485E)* allele (Figure S6A-C). Together, these data indicate that the defects
337 in lipid metabolism are independent of the abnormal DMP in *flr* mutants and further support the notion
338 that TWK-26 has a more direct role in intestinal metabolism.
339

340 **TWK-26 G485E restores intestinal dipeptide absorption in the *flr-4* and *flr-1* mutants**

341 Loss of DRL-1 or FLR-4 in the intestine causes a dietary restriction-like (DR-like) state, resulting
342 in small body size, slowed development, and impaired lipid accumulation (Chamoli et al. 2014; Katsura et
343 al. 1994; Torzone et al. 2023). Additionally, loss of *flr-1* results in a DR-like phenotype (Figure S1)
344 (Kaulich et al. 2022; Oishi et al. 2009; Take-uchi et al. 1998). Given the similarity between the mutant
345 phenotypes, it is likely that FLR-1, DRL-1, and FLR-4 act in the same pathway to maintain metabolic
346 homeostasis. Moreover, these DR-like phenotypes were partially suppressed by activating mutations in
347 the intestinal TWK-26 potassium channel (Figure 3), suggesting that impaired ion homeostasis may
348 underlie the DR-like phenotypes in these mutants. Given that the DR-like state of the *flr* mutants is not
349 coupled to the DMP, we explored the possibility that FLR-4 and FLR-1 may govern other ion-driven
350 processes in the intestine to coordinate metabolism, which when disrupted, could be restored by activation
351 of TWK-26. Intriguingly, intestinal nutrient absorption is an ion-dependent process, which could be
352 dysregulated in the *flr-4* and *flr-1* mutants, thereby contributing to the DR-like phenotypes. Mammalian
353 intestinal dipeptide transport via the PepT1 H^+-symporter is enhanced at low extracellular pH (Fei et al.
354 1994; Liang et al. 1995). Similarly, two *C. elegans* oligopeptide transporters, PEPT-1 and PEPT-2, display
355 proton gradient-driven electrogenic transport (Fei et al. 1998), with the activity of the intestinal PEPT-1
356 transporter strongly coupled to intracellular acidification. Importantly, loss of PEPT-1, or the downstream
357 intestinal Na^+/H^+ exchanger NHX-2, results in developmental delay and starvation phenotypes (Nehrke
358 2003). Furthermore, loss of the FLR-1 Na^+ channel impairs intestinal acidification and results in
359 starvation-like phenotypes (Figure S1 and Figure 4) (Kaulich et al. 2022).

360 Therefore, we reasoned that the *flr-4* and *flr-1* mutants may display defects in peptide absorption
361 due to impaired intestinal ion gradients. To test this hypothesis, we directly assessed amino acid
362 absorption by feeding animals β-Ala-Lys-AMCA, a fluorescent dipeptide that gets taken up in the gut
363 (Meissner et al. 2004). Interestingly, we observed a marked reduction in dipeptide absorption in the *flr-4*
364 and *flr-1* mutants (Figures 6A-B). These results demonstrate, for the first time, that the FLR-4/FLR-1

365 signaling axis is required for proper dipeptide absorption and provides a possible mechanism for the
366 starvation-like phenotypes that we observed in the *flr* mutants. Critically, the *twk-26(G485E)* mutation
367 strongly suppressed the dipeptide absorption defects in the *flr-4* and *flr-1* mutants, arguing that the TWK-
368 26 K2P promotes nutrient absorption when activated. Notably, loss of *gpla-1* also suppressed the
369 dipeptide absorption defects in the *flr-4* and *flr-1* mutants (Figures 6A-B), suggesting that neuronal signals
370 may regulate the activity of intestinal ion channels involved in amino acid absorption. We also observed
371 an intriguing spatial preference for TWK-26-dependent dipeptide uptake in the anterior intestine when
372 compared to the posterior intestine (Figure 6B), which is surprising given that *twk-26* expression is
373 significantly higher in the posterior intestine (Figures 2D-E). Together, these results suggest that the FLR-
374 4/FLR-1 pathway governs amino acid absorption by coordinating ion homeostasis alongside of the TWK-
375 26 K+ channel, possibly by directly, or indirectly, altering ion flux in the anterior intestine to maintain
376 intracellular acidification along the length of the intestine.

377 We could not neglect the possibility that absorption of other nutrients, in particular lipids, may
378 also be dependent on FLR-4, FLR-1, or TWK-26. Surprisingly, a *pept-1* mutation increases lipid uptake,
379 although this may be a compensatory mechanism in response to decreased amino acid absorption (Spanier
380 et al. 2009). To test this hypothesis, we fed animals C1-BODIPY-C12, a fluorescently-labeled fatty acid
381 derivative, to track lipid uptake in the intestine of the *flr-4* and *flr-1* mutants (O'Rourke et al. 2009; Sheng
382 et al. 2015; Spanier et al. 2009); however, we could not clearly resolve a reproducible phenotype and were
383 unable to establish a role for the FLR-4/FLR-1 pathway in lipid absorption using this approach.
384 Alternatively, we fed Nile Red, a lysochrome dye that accumulates in intestinal lipid droplets and
385 lysosome-related organelles following absorption (O'Rourke et al. 2009), to *flr-4* mutants. We found that
386 *flr-4* mutants displayed significantly less Nile Red signal in the intestine compared to the wild-type
387 control or the *flr-4 twk-26(G485E)* double mutant (Figure S7), indicating that *flr-4* may be required for
388 proper uptake of lipids or lipophilic molecules in the intestine.
389

390 **FLR-4 and TWK-26 balance intracellular and luminal pH to regulate nutrient absorption**

391 Loss of either PEPT-1, an intestinal oligopeptide transporter, or NHX-2, the intestinal Na^+/H^+
392 exchanger, impairs amino acid absorption, reduces growth rate, and restricts lipid accumulation (Meissner
393 et al. 2004; Nehrke 2003). Given that activation of TWK-26 suppressed these same defects in the *flr*
394 mutants, we hypothesized that the *twk-26(G485E)* mutation may also suppress loss of *pept-1* or *nhx-2*.
395 Although knock-down of *pept-1* or *nhx-2* by RNAi resulted in a dramatic reduction in P*vit-3::mCherry*
396 expression and small body sizes, these phenotypes were not suppressed by either the *twk-26(G485E)* or
397 *gpla-1* mutations (Figure S6A-C), suggesting that *twk-26*/*gpla-1* may function genetically upstream of
398 *pept-1*/*nhx-2* or in a different pathway altogether to suppress the metabolic defects of the *flr-4* and *flr-1*
399 mutants. We also tested whether the *flr* pathway was required for *pept-1*/*nhx-2* gene expression using
400 quantitative PCR, which surprisingly revealed that *pept-1* and *nhx-2* expression is strongly upregulated in
401 the *drl-1* or *flr-4* mutants (Figure S6D), possibly via compensatory mechanisms. Together, these results
402 suggest that the FLR-4 pathway may function independently of the canonical regulators of oligopeptide
403 absorption in the intestine.

404 It has been previously shown that *flr-1* is essential for intracellular intestinal pH oscillations and
405 that dysregulation of proton signaling upon loss of *flr-1* results in reduced fat storage (Kaulich et al.
406 2022). Thus, we hypothesized that *flr-4*, which functions in the same genetic pathway as *flr-1*, is also
407 required for proper intestinal pH oscillations, and consequently, proton gradient-driven dipeptide
408 absorption and intestinal lipid accumulation. Using the pHluorin sensor to measure intracellular pH (pHi)
409 in the intestine (Nehrke 2003), we found that the *flr-4* mutants displayed normal resting pHi between
410 contractions but relatively weak acidification concomitant with the DMP (Figure 7A-B). This observation
411 contrasts with the relatively acidic pHi observed in *nhx-2* and *vha-6* mutants, which also display DR-like
412 phenotypes (Nehrke 2003; Pfeiffer et al. 2008; Allman et al. 2009). We next wondered if pH oscillations
413 of the intestinal lumen, which are inversely correlated with changes in pHi, are also impacted by loss of
414 *flr-4*. Importantly, the intestinal lumen, which is thought to be the source of protons that drive intestinal

415 acidification and nutrient transport, is known to alkalinize during defecation (Pfeiffer et al. 2008). Thus,
416 we fed animals dextran-conjugated Oregon Green 488, a pH sensitive dye, to measure the fluid pH of the
417 intestinal lumen. We found that the *flr-4* mutant displayed a less acidic luminal pH and blunted luminal
418 pH oscillations in the posterior intestine relative to the wild-type control (Figure S8), consistent with
419 reduced proton-coupled nutrient uptake. In general, when the pBoc contraction is robust, the luminal
420 contents move from the posterior to anterior intestine and the luminal pH is consistent throughout the
421 length of the intestine. Interestingly, in the *flr-4* mutant, the luminal pH oscillations were restricted to the
422 posterior segment, with little movement of luminal contents, resulting in a pH gradient during contraction
423 (Figure 7C).

424 We then asked if activation of TWK-26 can resolve the defects in pH oscillations that we observed
425 in the *flr-4* mutants. While *twk-26(G485E)* was unable to suppress either resting or contracting pHi
426 defects of the *flr-4* mutant when measured independently, it was able to partly rescue the amplitude of the
427 pHi oscillations (Figure 7A-B). More notably, *twk-26(G485E)* suppressed some of the intestinal lumen pH
428 abnormalities in *flr-4* mutants. Specifically, activation of TWK-26 promotes alkalinization of the lumen in
429 the anterior (Figure 7C) but not in the posterior intestine (Figure S8). This decreases the difference
430 between the pH of the anterior and posterior lumens during defecation (Figure 7C), restoring a more wild-
431 type phenotype in the *flr-4* mutant. Together, these data reveal that both *flr-4* and *twk-26* are crucial for
432 regulating pH dynamics of intestinal cells and the gut lumen, providing new insight into the mechanisms
433 by which animals absorb nutrients and maintain metabolic homeostasis.

434

435 **DISCUSSION**

436 In this study, we establish a role for the TWK-26 potassium channel in governing lipid
437 homeostasis by promoting intestinal oligopeptide absorption in concert with the FLR-4 signaling pathway.
438 Loss of the FLR-4 kinase, or the downstream FLR-1 sodium channel, results in slow growth, small body
439 size, and reduced lipid accumulation, which likely results from impaired amino acid absorption. This

440 nutrient absorption defect causes a starvation-like state where the HLH-11/TFAP4 transcription factor is
441 likely degraded to initiate catabolic programs in the intestine. Remarkably, the DR-like state of the *flr-4*
442 and *flr-1* mutants is almost completely reversed by an activating mutation in the TWK-26 potassium leak
443 channel. Moreover, our study reveals a new mechanism by which the FLR-4 pathway and the TWK-26
444 potassium channel together coordinate oligopeptide absorption by altering intracellular and luminal pH
445 dynamics to maintain lipid homeostasis and license proper development.

446 In genetic models of dietary restriction, it is crucial to understand the specific molecular
447 mechanisms that reduce caloric intake and alter organismal physiology. Mutations in the DRL-1/FLR-4
448 signaling pathway confer DR-like phenotypes; however, the cause of these phenotypes remains poorly
449 understood (Chamoli et al. 2014; Take-uchi et al. 2005). The metabolic reprogramming stemming from
450 loss of *drl-1* includes increased beta-oxidation, reduced fat storage, and increased lifespan, which are all
451 characteristics of dietary restriction; however, the underlying mechanism has remained elusive (Chamoli
452 et al., 2014). Similarly, loss of FLR-4, which binds to DRL-1 in a complex (Torzone et al., 2023),
453 stimulates cytoprotective and detoxification pathways, which has also been observed in *drl-1* knock-down
454 animals (Chamoli et al. 2014, 2020; Verma et al. 2018).

455 Consistently, we demonstrate that loss of *flr-4* or *flr-1* results in a dramatic induction of autophagy
456 in the intestine, which has been previously observed during nutrient deprivation (Chamoli et al. 2014;
457 Hansen et al. 2008). HLH-30/TFEB is a conserved transcriptional regulator of autophagy that promotes
458 lysosomal biogenesis (Lapierre et al. 2013; Settembre et al. 2011). In the presence amino acids, mTORC1
459 is activated and phosphorylates TFEB, preventing its nuclear localization and restricting the induction of
460 autophagy programs (Martina et al. 2012; Roczniak-Ferguson et al. 2012; Sparta et al. 2023). It is possible
461 that signaling through mTORC1 is diminished in *flr-4* and *flr-1* mutants due to impaired absorption of
462 dipeptides (Hara et al. 1998). However, upon loss of *flr-4* and *flr-1*, we observed a decrease in nuclear
463 accumulation of HLH-30, which suggests that either mTORC1 signaling remains active or that *hlh-*
464 *30*/TFEB is transcriptionally or post-translationally down-regulated in these mutants through a different

465 mechanism. We find that HLH-11 levels are also severely decreased in the *flr* mutants. HLH-11 represses
466 the expression of lipid catabolism genes under fed conditions, causing lipid accumulation; however, HLH-
467 11 is degraded by proteosome upon starvation, promoting lipid utilization (Li et al. 2020). An intriguing
468 possibility is that both HLH-30 and HLH-11 are degraded in response to impaired FLR-4 signaling,
469 resulting in a nuanced transcriptional response that promotes catabolism and up-regulation of lysosomal
470 function; however, it is unclear which transcription factor(s) might contribute to this response. Still, it
471 remains critical to understand the mechanisms underlying this starvation-like response triggered by loss of
472 FLR-4 signaling.

473 Our discovery that activation of the TWK-26 potassium channel reversed the metabolic defects in
474 the *flr-4* and *flr-1* mutants provided, for the first time, an avenue for exploring the underlying mechanism
475 of the DR phenotypes associated with these mutations, as well as revealed how FLR-4 signaling
476 maintains metabolic homeostasis by governing ion-mediated processes in the intestine to promote growth.
477 Furthermore, we established a novel intestinal function for the TWK-26 leak channel, which has not been
478 previously characterized. KCNK3 is the mammalian ortholog of TWK-26 based on sequence similarity. In
479 mammals, KCNK3/TASK-1 is expressed in neurons (Talley et al. 2001) and forms homodimers or
480 heterodimers with other acid-sensitive TASK channels (Berg et al. 2004), such that these dimeric channels
481 are activated by extracellular alkalization and inhibited by acidification. Inhibition of TASK channels like
482 KCNK3, or its heterodimeric partner KCNK9, results in excitation of sensory neurons (Bautista et al.
483 2008). These acid-sensitive channels have also been described to regulate chemosensation in the carotid
484 body, which maintains normal respiratory ventilation (Trapp et al. 2008). Thus, TASK channels, like
485 KCNK3, play a crucial role in sensing changes in their environment to maintain homeostasis. While
486 KCNK3 is known to be expressed in the human intestine (Duprat et al. 1997), a functional role in nutrient
487 absorption has not yet been described. Thus, our findings on TWK-26 provide the molecular framework
488 to dissect the metabolic role of KCNK3 in humans.

489 Furthermore, we elucidated the mechanism by which the TWK-26 potassium channel maintains
490 metabolic homeostasis. We demonstrate that the G485E mutation, which genocopies the gain-of-function
491 TM2.6 mutation (Ben Soussia et al. 2019), likely increases TWK-26 channel activity to promote robust
492 oligopeptide absorption, a function that has not been previously ascribed to KCNK3. It remains elusive
493 how the G485E mutation activates the TWK-26 channel, especially given that the C-terminus is necessary
494 for TWK-26 G485E activity. We have identified residues in the C-terminus that may serve as potential
495 phosphorylation sites (O'Kelly et al. 2002), so it is possible that phosphorylation of the TWK-26 C-
496 terminus is required for channel activation.

497 It is commonly accepted that the *C. elegans* intestine, which is comprised of 20 epithelial cells, is
498 simplistic and uniform, given that each intestinal cell has arisen from a single progenitor (Zhang et al.
499 2017; Sulston et al. 1983; Asan et al. 2016). We found that expression of *twk-26* is restricted to the
500 posterior intestine. Little is known about anterior-posterior gene expression patterning in the *C. elegans*
501 intestine, although some studies suggest that this spatial patterning may be governed by Wnt signaling
502 (Schroeder and McGhee 1998; Fukushige et al. 2005). Intriguingly, expression of the *pho-1* acid
503 phosphatase, which is required to promote proper growth, is also limited to the posterior intestine
504 (Fukushige et al. 2005). Thus, it is possible that anterior-posterior gene expression patterning in the
505 intestine governs nutrient absorption differently along the length of the intestine. In support of this idea,
506 activation of TWK-26 strongly promotes dipeptide absorption in the anterior intestine while the *flr-4* and
507 *flr-1* mutants display a decrease in oligopeptide absorption in the posterior intestine. It is possible that the
508 activity of TWK-26 G485E in the posterior intestine is sufficient to promote mixing of luminal contents
509 throughout the length of the intestine, thereby driving robust dipeptide absorption in the anterior intestinal
510 cells.

511 Consistent with this idea, we found that activation of TWK-26 promotes alkalinization in the
512 lumen of the anterior intestine and partially suppresses the impaired intestinal acidification observed in
513 the *flr-4* mutant. Nutrient absorption in the intestine is driven by a pH gradient across the apical

514 membrane, where acidification of the intestinal lumen enhances the uptake of dipeptides and increases fat
515 accumulation (Allman et al. 2009; Nehrke 2003). Yet, it remains unclear how anterior lumen
516 alkalinization is functionally tied to the robust oligopeptide absorption that we observe upon activation of
517 TWK-26. It is possible that TWK-26 has indirect effects on these intestinal ion gradients. Notably,
518 extracellular alkalinization has been shown to activate other TASK channels (Lotshaw 2006; Reyes et al.
519 1998; Niemeyer et al. 2007), which may more directly stabilize membrane ion gradients necessary for
520 proper nutrient absorption.

521 While the ion gradients that regulate the defecation motor program have been previously linked to
522 fatty acid absorption (Spanier et al. 2009), we found that TWK-26 is more directly involved in nutrient
523 absorption and that its activity can be uncoupled from the defecation motor program (DMP). Indeed,
524 activation of TWK-26 failed to suppress the defecation defects of the *flr* mutants, namely the shortened
525 defecation interval and expulsion defects. This result is surprising, given that the DMP plays a central role
526 in nutrient absorption, proper growth, and lipid metabolism (Kaulich et al. 2023; Suzuki et al. 2022).
527 Moreover, TWK-26 activation also failed to suppress the intestinal bloating phenotype of the *flr* mutants,
528 which has been observed in other DR mutants (Das et al. 2023; Katsura et al. 1994; Long et al. 2002).
529 Notably, mTOR pathway mutants also display luminal bloating (Long et al. 2002; Meissner et al. 2004),
530 which is further enhanced by mutation of the dipeptide transporter *pept-1* (Meissner et al. 2004),
531 suggesting that intestinal distension may be a consequence of nutrient deprivation. Intestinal bloating is
532 also observed during pathogen infection (Irazoqui et al. 2010; Singh and Aballay 2019), which
533 upregulates an immune response and alters feeding behaviors in *C. elegans*. Immune signaling through
534 the p38/PMK-1 MAPK pathway is hyperactive in the *drl-1* mutant, restricting growth and down-
535 regulating vitellogenesis (Torzone et al. 2023). Consistently, we observed TIR-1 aggregation in the *flr-4*
536 mutant. However, hyperactivation of TWK-26 does not suppress TIR-1 puncta formation nor intestinal
537 bloating, suggesting that restoration of ion homeostasis in the intestine promotes lipid accumulation and
538 growth independently of altering innate immunity pathways. Excitingly, our findings uniquely uncouple

539 intestinal distension and the DMP from metabolic homeostasis, suggesting that animals may be able to
540 dynamically alter the expression of factors that maintain ion homeostasis to promote efficient uptake and
541 utilization of nutrients.

542 The FLR-4 pathway supports growth and reproduction by altering intracellular and intestinal
543 lumen pH dynamics to promote the absorption of oligopeptides in the intestine. When signaling through
544 this axis is impaired, animals fail to develop at a normal rate and exhibit a reduction in fat storage and
545 maternal vitellogenin provisioning. Importantly, hyperactivation of the TWK-26 potassium leak channel
546 restores intestinal homeostasis to support normal growth by increasing nutrient absorption, likely by
547 balancing the ion gradients that govern proton-driven dipeptide transport. This work establishes a
548 platform to investigate how protein kinase signaling maintains metabolic homeostasis to promote
549 development and enhances our understanding of how ion channels govern lipid metabolism, which could
550 be important in unraveling the mechanisms of metabolic diseases like diabetes and inflammatory bowel
551 disease.

552

553 **METHODS**
554
555 ***C. elegans* strains**

556 *C. elegans* strains were maintained on NGM media plates seeded with *E. coli* OP50 at 20°C as previously
557 described (Brenner 1974). Animals were synchronized at the L1 larval stage by isolating embryos via
558 bleaching followed by incubation overnight at room temperature in M9 buffer. Auxin inducible
559 degradation (AID) experiments were performed using plates containing 4mM naphthaleneacetic acid (K-
560 NAA, PhytoTech). All strains used in this study are listed in Supplementary Table S1.

561

562 **Generation of transgenic animals**

563 To generate the P*twk-26::mCherry::unc-54* transgene, the promoter of *twk-26* (chromosome X: 3,055,393
564 – 3,054,414; WS295) was amplified from genomic DNA and fused to a *mCherry::unc-54 3'UTR*

565 fragment via PCR fusion (Hobert 2002). The resulting PCR fragment was microinjected *unc-119(ed3)*
566 animals at 20ng/µl, along with 5ng/µl P*myo-3::GFP*, 20ng/µl pCFJ151, and 55ng/µl of 2-Log DNA ladder
567 (New England BioLabs), to generate the DLS1045 strain. Transgenic animals were imaged on a Nikon
568 SMZ-18 Stereo microscope equipped with a DS-Qi2 monochrome camera. Additional independent array
569 lines were generated and displayed a similar distribution of mCherry signal in the intestine.
570
571 **CRISPR/Cas9 gene editing**
572 Genomic editing was conducted by germline microinjection of Cas9::crRNA::tracrRNA complexes
573 (Integrated DNA Technologies) as previously described (Ghanta and Mello 2020). crRNA sequences are
574 listed in Supplementary Table S2. Missense mutations were generated using single-stranded
575 oligodeoxynucleotides as the repair donor molecule. To create the *twk-26* C-terminal deletion, a crRNA
576 was designed for each end of the deletion site and a single-stranded repair oligo bridged the repair site,
577 which resulted in a frameshift mutation at Thr502. To insert the 2xmIAA7::3xHA or the SL2::H2B::GFP
578 cassette into the 3' end of the *twk-26* locus, dsDNA donor molecules with ~40 bp homology arms were
579 prepared by PCR using Q5 DNA Polymerase (New England BioLabs) and were purified with HighPrep
580 PCR Clean-up beads (MagBio) per the manufacturer's instructions. Prior to microinjection, the DNA
581 repair template was melted and reannealed (Ghanta and Mello 2020).
582
583 **RNAi experiments**
584 *E. coli* HT115(DE3) strains carrying the control pL4440 vector or gene-specific RNAi plasmids (Ahringer
585 RNAi library) were grown for ~20 hours in Luria-Bertani media with 100µg/mL ampicillin at 37°C.
586 Bacteria were concentrated 30x via centrifugation and seeded onto NGM plates containing 5mM
587 isopropyl-β-D-thiogalactoside (IPTG) and 50µg/ml ampicillin. Plates were maintained at room
588 temperature overnight to induce dsRNA expression. Synchronized L1 animals were dropped on RNAi
589 plates and were grown to day 1 of adulthood.

590

591 **Oil Red O staining**

592 Approximately 150 L4 animals were picked to new plates, grown for 24 hours, and harvested as day 1
593 adults in S-basal media. Animals were washed in S-basal, fixed with 60% isopropanol, and stained for 7
594 hours with 0.5% Oil Red O as previously described (Dowen 2019). Animals were mounted on 2% agarose
595 pads and imaged using a Nikon SMZ-18 Stereo microscope equipped with a DS-Qi2 monochrome camera
596 for intensity analyses or a Nikon Ti2 widefield microscope equipped with a DS-Fi3 camera for
597 representative color images. Quantification of Oil Red O staining was conducted by manually outlining
598 individual animals in Fiji (Schindelin et al. 2012) and then measuring the mean gray value within the area.
599 These values were subtracted from the maximum gray value for 16-bit images, 65,526, as previously
600 described (DuMez-Kornegay et al. 2024). Data were plotted and analyzed using Prism 9. A one-way
601 ANOVA with a Bonferroni correction was used to calculate *P* values.

602

603 **Nile Red staining**

604 A Nile Red stock solution was prepared in acetone at 0.5mg/mL and stored at 4°C. Approximately 150 L4
605 animals were picked to new plates and harvested 24 hours later as day 1 adults in S-basal media. Animals
606 were washed, fixed in 60% isopropanol, and stained for 2 hours in 0.03mg/mL Nile Red. Animals were
607 mounted on 2% agarose pads and imaged with a Nikon Ti2 widefield microscope equipped with a
608 Hamamatsu ORCA-Fusion BT camera. Quantification of fluorescence intensity was conducted by
609 manually outlining individual animals in Fiji and measuring the average pixel intensity within the area.
610 Values were plotted, and statistical analyses were performed, using Prism 9. A one-way ANOVA was
611 conducted with Bonferroni corrections to calculate *P* values.

612

613 **Growth and body size assays**

614 For developmental growth rate assays, animals were grown for several generations without starvation
615 prior to being assayed. Approximately 100-200 freshly laid embryos (20 hours or less) were picked to
616 new plates and scored every 24 hours for 7 days. Gravid adults were removed from the population and
617 were recorded as having reached adulthood. For the single time point developmental assays (Figure 2A
618 and 2C), animals were grown from synchronized L1s on RNAi plates and the developmental stage for
619 each worm was recorded at the indicated time point across the entire population.
620 To quantify body size, animals were picked at the L4 larval stage to new plates and maintained for
621 24 hours prior to imaging. Day 1 adult animals were mounted on 2% agarose pads with 25mM levamisole
622 and imaged using a Nikon SMZ-18 stereo microscope equipped with a DS-Qi2 monochrome camera.
623 Body size values were obtained by manually outlining individual worms in Fiji, the area measurements
624 (pixels) were converted to mm^2 using known imaging parameters, and the data were plotted and analyzed
625 in Prism 9 (one-way ANOVA with a Bonferroni correction for multiple testing).
626
627 **Quantitative PCR**
628 Preparation of total RNA and qPCR assays were performed exactly as previously described (Torzone et al.
629 2023). All primer sequences are listed in Supplementary Table S3.
630
631 **EMS Mutagenesis**
632 Mutagenesis of *flr-4(ut7); mgIs70[*P*vit-3::GFP]* animals was performed using 47mM ethyl
633 methanesulfonate (EMS, Sigma-Aldrich) and was conducted as previously described (Dowen et al. 2016).
634 Approximately 330,000 haploid genomes were screened on *flr-4* RNAi plates, which prevented isolation
635 of intragenic suppressor mutations. The *flr-4* suppressor strains were isolated in the F1 generation based
636 on increased growth rate and/or P*vit-3::GFP* reporter expression relative to the non-mutagenized *flr-*
637 *4(ut7); mgIs70* strain. Suppressor strains were backcrossed to the parental strain four times, the genomic
638 DNA was isolated using the Qiagen Gentra Puregene Tissue Kit (Doitsidou et al. 2010), and libraries for

639 whole genome sequencing were prepared and sequenced by Novogene (Sacramento, CA) using an
640 Illumina NovaSeq instrument (PE 150). Candidate suppressor mutations were identified using in-house
641 scripts, as previously described (Minevich et al. 2012).
642
643 **Reporter imaging and quantification**
644 Strains carrying either the high-copy *mgIs70[*P*vit-3::GFP]* transgene or the single-copy *rhdSi42[*P*vit-*
645 *3::mCherry]* transgene have been previously described (Dowen et al. 2016; Torzone et al. 2023). P*vit-*
646 *3::mCherry* fluorescence was measured in strains containing the *rhdSi42* reporter. Animals were grown to
647 the L4 stage, picked to new plates, and imaged 24 hours later as day 1 adults on a 2% agarose pads
648 containing 25mM levamisole. A Nikon SMZ-18 Stereo microscope equipped with a DS-Qi2 monochrome
649 camera was used for imaging. In Fiji, the body of each animal was manually outlined in the bright field
650 channel and the mean intensity values were obtained in the mCherry channel. The values were plotted in
651 Prism 9 and a one-way ANOVA with a Bonferroni correction for multiple testing was conducted to obtain
652 *P* values.
653 To determine the cellular localization of the HLH-30::GFP and HLH-11::GFP transcription
654 factors, strains containing the *sqIs19[HLH-30::GFP]* or *wgIs396[HLH-11::TY1::EGFP::3xFLAG]*
655 transgenes were grown on RNAi plates until the L4 stage, picked to fresh RNAi plates, and imaged 24
656 hours later as day 1 adults on 2% agarose pads with levamisole using a Nikon Ti2 widefield microscope
657 equipped with a Hamamatsu ORCA-Fusion BT camera. A 10x objective was used to capture
658 representative images and a 20x objective was used to image animals for fluorescence measurements. For
659 each genotype, quantification of nuclear fluorescence was performed by outlining the 2 posterior-most
660 intestinal nuclei for 30 animals and measuring the mean intensity value in Fiji. Mean fluorescence
661 intensity values were plotted in Prism 9 and a one-way ANOVA with a Bonferroni correction for multiple
662 testing was conducted to obtain *P* values.

663 The *sqIs11[mCherry::GFP::LGG-1]* reporter was used to measure autophagic lysosomes (Chang
664 et al. 2017). Imaging was conducted using a CFI Apo 60X Oil TIRF objective on a Nikon Ti2 widefield
665 microscope equipped with a Hamamatsu ORCA-Fusion BT camera. Animals were grown to the L4 stage
666 on RNAi plates and transferred to freshly made RNAi plates 24 hours prior to imaging. Day 1 adult
667 animals were mounted on 2% agarose pads with levamisole and the posterior-most intestinal cells were
668 imaged in the bright field, mCherry, and FITC channels. Autophagic lysosomes were measured in the
669 posterior intestine where the last 2-4 cells are unobstructed by other tissues. Z-stacks were cropped to
670 0.6mm to capture planes of the intestine that were easily visualized. Z-stacks were then denoised,
671 deconvoluted, and compressed into a single image using the Nikon NIS-Elements analysis software.
672 Hand-drawn ROIs were placed around the 2-4 posterior-most intestinal cells and mCherry puncta were
673 measured using the object counts feature in NIS-elements. Counts of LGG-1::mCherry puncta and the
674 puncta area relative to the ROI area were plotted in Prism 9 and a one-way ANOVA with a Bonferroni
675 correction was performed to calculate *P* values.
676 To measure intestinal lumen widths, the *erm-1(mib15[erm-1::eGFP])* strain was used to mark the
677 intestinal lumen (Ramalho et al. 2020). Animals were grown on RNAi plates, picked at the L4 larval stage
678 to fresh RNAi plates, and imaged 24 hours later as day 1 adults mounted on 2% agarose pads containing
679 levamisole. A Nikon Ti2 widefield microscope equipped with a Hamamatsu ORCA-Fusion BT camera
680 was used to image animals at 20x. Intestinal lumen widths were measured in the middle of the animal
681 where the intestine was not obstructed by other tissues. Lumen widths from 30 animals were obtained for
682 each condition, the data were plotted in Prism 9, and a one-way ANOVA with a Bonferroni correction was
683 performed to calculate *P* values.
684
685 **Nutrient absorption assays**
686 Nile Red feeding was performed as previously described (Mak et al. 2006) with only minor
687 modifications. Briefly, embryos or L1 animals were picked to Nile Red-containing plates (500µL of

688 1μg/mL Nile Red solution overlaid onto the bacterial lawns), grown to day 1 of adulthood, mounted on
689 2% agarose pads containing levamisole, and imaged at 8x zoom using a Nikon SMZ-18 Stereo
690 microscope with a DS-Qi2 monochrome camera using the mCherry and DIC channels.
691 For dipeptide absorption assays, feeding with β-Ala-Lys-AMCA (BioSynth) was performed as
692 previously described (Meissner et al. 2004). Briefly, animals were grown to the L4 stage, picked to fresh
693 plates, grown for 24 hours, and transferred to 0.5mL Eppendorf tubes containing 1mM β-Ala-Lys-AMCA
694 in 100μL of M9 media. The samples were covered in aluminum foil, incubated for 3 hours at room
695 temperature with gentle rocking, washed three times with M9, and mounted on 2% agarose pads
696 containing levamisole for imaging with a Nikon Ti2 widefield microscope equipped with a Hamamatsu
697 ORCA-Fusion BT camera. Using Fiji, whole animals or a specific body regions (*i.e.*, anterior, posterior)
698 were outlined in the brightfield channel and the mean fluorescence measurements were measured in the
699 DAPI channel. The values were plotted in Prism 9 and a one-way ANOVA with a Bonferroni correction
700 for multiple testing was conducted to obtain the *P* values.
701
702 **Defecation assays**
703 Videos of day 1 adult animals were recorded using a Nikon SMZ-18 Stereo microscope with a DS-Qi2
704 monochrome camera. Animals were permitted to freely move and feed on *E. coli* OP50 NGM plates while
705 recording. One animal at a time was recorded for a total of 5 complete defecation cycles, each one marked
706 by a posterior body wall contraction (pBoc) (Iwasaki et al. 1995; Liu and Thomas 1994). The time
707 interval between pBoc events was recorded as the DMP interval, and the number of expulsion (exp)
708 events observed during the 5 recorded defecation cycles were noted. Animals were removed from the
709 plate after recording to ensure that 10 unique individuals were assayed per strain. Data were plotted in
710 Prism 9 and a one-way ANOVA was performed with a Bonferroni correction for multiple testing to
711 calculate *P* values.
712

713 **Pharyngeal pumping assays**

714 One-minute videos of 10 unique day 1 adult animals per genotype were recorded using a Nikon SMZ-18
715 Stereo microscope with a DS-Qi2 monochrome camera. Animals were permitted to freely move and feed
716 on *E. coli* OP50 NGM plates during each recording. The number of pharyngeal pumps per minute were
717 measured by reducing the video speed by 50% while counting. Data were plotted in Prism 9 and a one-
718 way ANOVA was performed with a Bonferroni correction for multiple testing to calculate *P* values.

719

720 **Imaging and analysis of intracellular pH and intestinal lumen pH**

721 For intracellular pH imaging, day 1 adult transgenic animals expressing pHluorin (Miesenböck et al.
722 1998) under the control of the pan-intestinal *nhx-2* promoter were used to visualize changes in
723 intracellular pH, as previously described (Nehrke 2003).

724 The luminal pH measurements were obtained using Oregon Green, as previously described
725 (Allman et al. 2009). Briefly, day 1 adults were washed from their plates and pelleted by brief
726 centrifugation. The animals were resuspended in S-basal buffer with bacterial food to a final volume of
727 50µL, and an additional 50µL of S-basal containing 5mg/ml of an Oregon Green-dextran conjugate (70
728 kDa, Molecular Probes) was added. The worms were loaded with the conjugate by feeding for 2 hours at
729 20°C on a rocking platform and returned to NGM plates seeded with *E. coli* OP50 for imaging. The
730 fluorescence excitation ratio was converted to pH using an *in vitro* calibration curve for the dye in
731 solution.

732 For both assays, the plates were inverted onto the stage of a Nikon Eclipse TE2000-S microscope
733 (Nikon Instruments), and freely moving subjects were kept within the field of view manually via stage
734 manipulation. Illumination was provided by a Polychrome IV monochromator (TILL Photonics).
735 Emissions were collected on a high-speed charge-coupled device camera (PCO Imaging). pH was
736 assessed via dual excitation ratio spectroscopy, with sequential 10ms excitation at 410 and 470nm with
737 535nm emissions (pHluorin, intracellular pH) or sequential 10ms excitation at 440 and 490nm with

535nm emissions (Oregon Green-dextran, luminal pH). A 2×2 binning approach was utilized to increase signal to noise. Background subtraction was performed pixel-by-pixel at each excitation wavelength using images acquired from seeded plates lacking worms. Ratio images were further refined by thresholding, with the lowest intensity pixels (generally <2% of the data) set to zero. For quantitative analysis, fluorescence ratios were converted to pH using a Boltzmann equation and a calibration curve generated by *ex vivo* intestinal perfusion with a high K^+/nigericin solution. TILLvisION software (TILL Photonics) was used for data analysis. Data were plotted using Prism 8.

Raw data

The underlying numerical data and sample sizes for each individual experiment can be found in S1 Data.

AUTHOR CONTRIBUTIONS

S.K.T., T.C., K.W.N., and R.H.D. designed the experiments. S.K.T., P.C.B., T.C., N.R.C., K.N.S., and K.R.V. performed the experiments. S.K.T., T.C., K.W.N., K.N.S., and R.H.D. interpreted the results. S.K.T. prepared the original draft of the manuscript. S.K.T., T.C., K.W.N., and R.H.D. reviewed and edited the manuscript. R.H.D. and K.W.N. secured funding for the study.

FUNDING

This study was supported by the National Institute of General Medical Sciences grant R35GM137985 to R.H.D and National Institute of Aging grant R01AG067617 to K.W.N.

ACKNOWLEDGEMENTS

The *Caenorhabditis* Genetics Center provided some of the strains used in this study, which is supported by the NIH Office of Research Infrastructure Programs (P40 OD010440).

763 **CONFLICT OF INTEREST**

764 The authors declare no competing interests.

765

766 **REFERENCES**

767 Al-Hazza A, Linley JE, Aziz Q, MacLennan KA, Hunter M, Sandle GI. 2012. Potential role of reduced
768 basolateral potassium (IKCa3.1) channel expression in the pathogenesis of diarrhoea in ulcerative
769 colitis. *J Pathol* **226**: 463–470.

770 Allman E, Johnson D, Nehrke K. 2009. Loss of the apical V-ATPase a-subunit VHA-6 prevents
771 acidification of the intestinal lumen during a rhythmic behavior in *C. elegans*. *Am J Physiol-Cell*
772 *Physiol* **297**: C1071–C1081.

773 Anderson KJ, Cormier RT, Scott PM. 2019. Role of ion channels in gastrointestinal cancer. *World J*
774 *Gastroenterol* **25**: 5732–5772.

775 Asan A, Raiders SA, Priess JR. 2016. Morphogenesis of the C. elegans Intestine Involves Axon Guidance
776 Genes. *PLoS Genet* **12**: e1005950.

777 Avery L. 1993. The genetics of feeding in Caenorhabditis elegans. *Genetics* **133**: 897–917.

778 Bautista DM, Sigal YM, Milstein AD, Garrison JL, Zorn JA, Tsuruda PR, Nicoll RA, Julius D. 2008.
779 Pungent agents from Szechuan peppers excite sensory neurons by inhibiting two-pore potassium
780 channels. *Nat Neurosci* **11**: 772–779.

781 Ben Soussia I, El Mouridi S, Kang D, Leclercq-Blondel A, Khoubza L, Tardy P, Zariohi N, Gendrel M,
782 Lesage F, Kim E-J, et al. 2019. Mutation of a single residue promotes gating of vertebrate and
783 invertebrate two-pore domain potassium channels. *Nat Commun* **10**: 787.

784 Berg AP, Talley EM, Manger JP, Bayliss DA. 2004. Motoneurons express heteromeric TWIK-related acid-
785 sensitive K+ (TASK) channels containing TASK-1 (KCNK3) and TASK-3 (KCNK9) subunits. *J*
786 *Neurosci Off J Soc Neurosci* **24**: 6693–6702.

787 Branicky R, Hekimi S. 2006. What keeps C. elegans regular: the genetics of defecation. *Trends Genet* **22**:
788 571–579.

789 Brenner S. 1974. The genetics of Caenorhabditis elegans. *Genetics* **77**: 71–94.

790 Chamoli M, Goyala A, Tabrez SS, Siddiqui AA, Singh A, Antebi A, Lithgow GJ, Watts JL,
791 Mukhopadhyay A. 2020. Polyunsaturated fatty acids and p38-MAPK link metabolic
792 reprogramming to cytoprotective gene expression during dietary restriction. *Nat Commun* **11**:
793 4865.

794 Chamoli M, Singh A, Malik Y, Mukhopadhyay A. 2014. A novel kinase regulates dietary restriction-
795 mediated longevity in Caenorhabditis elegans. *Aging Cell* **13**: 641–655.

796 Chang JT, Kumsta C, Hellman AB, Adams LM, Hansen M. 2017. Spatiotemporal regulation of autophagy
797 during Caenorhabditis elegans aging. *eLife* **6**: e18459.

798 Cully D, Cohen NR, Breen PC, Newman MA, Dowen RH. 2024. A novel gain-of-function mutation in
799 sgk-1 partially suppresses mTORC2 defects. *MicroPublication Biol* **2024**.

800 Dal Santo P, Logan MA, Chisholm AD, Jorgensen EM. 1999. The inositol trisphosphate receptor regulates
801 a 50-second behavioral rhythm in C. elegans. *Cell* **98**: 757–767.

802 Das P, Aballay A, Singh J. 2023. Calcineurin inhibition enhances Caenorhabditis elegans lifespan by
803 defecation defects-mediated calorie restriction and nuclear hormone signaling.
804 https://elifesciences.org/reviewed-preprints/89572v1 (Accessed May 1, 2024).

805 Doitsidou M, Poole RJ, Sarin S, Bigelow H, Hobert O. 2010. C. elegans Mutant Identification with a
806 One-Step Whole-Genome-Sequencing and SNP Mapping Strategy ed. A.C. Hart. *PLoS ONE* **5**:
807 e15435.

808 Dowen RH. 2019. CEH-60/PBX and UNC-62/MEIS Coordinate a Metabolic Switch that Supports
809 Reproduction in C. elegans. *Dev Cell* **49**: 235-250.e7.

810 Dowen RH, Breen PC, Tullius T, Conery AL, Ruvkun G. 2016. A microRNA program in the *C. elegans*
811 hypodermis couples to intestinal mTORC2/PQM-1 signaling to modulate fat transport. *Genes Dev*
812 **30**: 1515–1528.

813 DuMez-Kornegay RN, Baker LS, Morris AJ, DeLoach WLM, Dowen RH. 2024. Kombucha Tea-
814 associated microbes remodel host metabolic pathways to suppress lipid accumulation. *PLoS Genet*
815 **20**: e1011003.

816 Duprat F, Lesage F, Fink M, Reyes R, Heurteaux C, Lazdunski M. 1997. TASK, a human background K+
817 channel to sense external pH variations near physiological pH. *EMBO J* **16**: 5464–5471.

818 Espelt MV, Estevez AY, Yin X, Strange K. 2005. Oscillatory Ca2+ signaling in the isolated
819 Caenorhabditis elegans intestine: role of the inositol-1,4,5-trisphosphate receptor and
820 phospholipases C beta and gamma. *J Gen Physiol* **126**: 379–392.

821 Estevez AY, Strange K. 2005. Calcium feedback mechanisms regulate oscillatory activity of a TRP-like
822 Ca2+ conductance in C. elegans intestinal cells. *J Physiol* **567**: 239–251.

823 Fei YJ, Fujita T, Lapp DF, Ganapathy V, Leibach FH. 1998. Two oligopeptide transporters from
824 Caenorhabditis elegans: molecular cloning and functional expression. *Biochem J* **332 (Pt 2)**: 565–
825 572.

826 Fei Y-J, Kanai Y, Nussberger S, Ganapathy V, Leibach FH, Romero MF, Singh SK, Boron WF, Hediger
827 MA. 1994. Expression cloning of a mammalian proton-coupled oligopeptide transporter. *Nature*
828 **368**: 563–566.

829 Feliciangeli S, Chatelain FC, Bichet D, Lesage F. 2015. The family of K2P channels: salient structural and
830 functional properties. *J Physiol* **593**: 2587–2603.

831 Fukushige T, Goszczynski B, Yan J, McGhee JD. 2005. Transcriptional control and patterning of the pho-
832 1 gene, an essential acid phosphatase expressed in the C. elegans intestine. *Dev Biol* **279**: 446–
833 461.

834 Ghanta KS, Mello CC. 2020. Melting dsDNA Donor Molecules Greatly Improves Precision Genome
835 Editing in Caenorhabditis elegans. *Genetics* **216**: 643–650.

836 Gottschling D-C, Döring F, Lüersen K. 2017. Locomotion Behavior Is Affected by the GαS Pathway and
837 the Two-Pore-Domain K+ Channel TWK-7 Interacting in GABAergic Motor Neurons in
838 Caenorhabditis elegans. *Genetics* **206**: 283–297.

839 Gruss M, Corsi AK. 2022. Using Caenorhabditis elegans as a Model for Mechanistic Insights of
840 Craniofacial Development. *Methods Mol Biol Clifton NJ* **2403**: 1–18.

841 Hansen M, Chandra A, Mitic LL, Onken B, Driscoll M, Kenyon C. 2008. A role for autophagy in the
842 extension of lifespan by dietary restriction in C. elegans. *PLoS Genet* **4**: e24.

843 Hara K, Yonezawa K, Weng QP, Kozlowski MT, Belham C, Avruch J. 1998. Amino acid sufficiency and
844 mTOR regulate p70 S6 kinase and eIF-4E BP1 through a common effector mechanism. *J Biol*
845 *Chem* **273**: 14484–14494.

846 Hobert O. 2002. PCR fusion-based approach to create reporter gene constructs for expression analysis in
847 transgenic C. elegans. *BioTechniques* **32**: 728–730.

848 Hobert O. 2013. The neuronal genome of Caenorhabditis elegans. *WormBook Online Rev C Elegans Biol*
849 1–106.

850 Honey KL, Torzone SK, Dowen RH. 2023. The C. elegans flr-3(ut9) mutation is a loss-of-function
851 insertion within the drl-1 locus. *MicroPublication Biol* **2023**.

852 Irazoqui JE, Troemel ER, Feinbaum RL, Luhachack LG, Cezairliyan BO, Ausubel FM. 2010. Distinct
853 pathogenesis and host responses during infection of C. elegans by P. aeruginosa and S. aureus.
854 *PLoS Pathog* **6**: e1000982.

855 Iwasaki K, Liu DW, Thomas JH. 1995. Genes that control a temperature-compensated ultradian clock in
856 Caenorhabditis elegans. *Proc Natl Acad Sci U S A* **92**: 10317–10321.

857 Katsura I, Kondo K, Amano T, Ishihara T, Kawakami M. 1994. Isolation, characterization and epistasis of
858 fluoride-resistant mutants of Caenorhabditis elegans. *Genetics* **136**: 145–154.

859 Kaulich E, Carroll T, Ackley BD, Tang Y-Q, Hardege I, Nehrke K, Schafer WR, Walker DS. 2022.
860 Distinct roles for two Caenorhabditis elegans acid-sensing ion channels in an ultradian clock. *eLife*
861 **11**: e75837.

862 Kaulich E, Grundy LJ, Schafer WR, Walker DS. 2023. The diverse functions of the DEG/ENaC family:
863 linking genetic and physiological insights. *J Physiol* **601**: 1521–1542.

864 Kimble J, Sharrock WJ. 1983. Tissue-specific synthesis of yolk proteins in Caenorhabditis elegans. *Dev*
865 *Biol* **96**: 189–196.

866 Kobayashi Y, Kimura KD, Katsura I. 2011. Ultradian rhythm in the intestine of Caenorhabditis elegans is
867 controlled by the C-terminal region of the FLR-1 ion channel and the hydrophobic domain of the
868 FLR-4 protein kinase: Ultradian clock regulated by ion channel. *Genes Cells* **16**: 565–575.

869 Kumar S, Egan BM, Kocsisova Z, Schneider DL, Murphy JT, Diwan A, Kornfeld K. 2019. Lifespan
870 Extension in C. elegans Caused by Bacterial Colonization of the Intestine and Subsequent
871 Activation of an Innate Immune Response. *Dev Cell* **49**: 100-117.e6.

872 Lakowski B, Hekimi S. 1998. The genetics of caloric restriction in Caenorhabditis elegans. *Proc Natl*
873 *Acad Sci U S A* **95**: 13091–13096.

874 Lapierre LR, De Magalhaes Filho CD, McQuary PR, Chu C-C, Visvikis O, Chang JT, Gelino S, Ong B,
875 Davis AE, Irazoqui JE, et al. 2013. The TFEB orthologue HLH-30 regulates autophagy and
876 modulates longevity in Caenorhabditis elegans. *Nat Commun* **4**: 2267.

877 Li Y, Ding W, Li C-Y, Liu Y. 2020. HLH-11 modulates lipid metabolism in response to nutrient
878 availability. *Nat Commun* **11**: 5959.

879 Liang R, Fei YJ, Prasad PD, Ramamoorthy S, Han H, Yang-Feng TL, Hediger MA, Ganapathy V, Leibach
880 FH. 1995. Human intestinal H+/peptide cotransporter. Cloning, functional expression, and
881 chromosomal localization. *J Biol Chem* **270**: 6456–6463.

882 Lin-Moore AT, Oyeyemi MJ, Hammarlund M. 2021. rab-27 acts in an intestinal pathway to inhibit axon
883 regeneration in C. elegans ed. G.P. Copenhaver. *PLOS Genet* **17**: e1009877.

884 Liu DW, Thomas JH. 1994. Regulation of a periodic motor program in C. elegans. *J Neurosci Off J Soc*
885 *Neurosci* **14**: 1953–1962.

886 Long X, Spycher C, Han ZS, Rose AM, Müller F, Avruch J. 2002. TOR Deficiency in C. elegans Causes
887 Developmental Arrest and Intestinal Atrophy by Inhibition of mRNA Translation. *Curr Biol* **12**:
888 1448–1461.

889 Lotshaw DP. 2006. Biophysical and Pharmacological Characteristics of Native Two-Pore Domain TASK
890 Channels in Rat Adrenal Glomerulosa Cells. *J Membr Biol* **210**: 51–70.

891 Lu X, Luo C, Wu J, Deng Y, Mu X, Zhang T, Yang X, Liu Q, Li Z, Tang S, et al. 2023. Ion channels and
892 transporters regulate nutrient absorption in health and disease. *J Cell Mol Med* **27**: 2631–2642.

893 Magalhães D, Cabral JM, Soares-da-Silva P, Magro F. 2016. Role of epithelial ion transports in
894 inflammatory bowel disease. *Am J Physiol Gastrointest Liver Physiol* **310**: G460-476.

895 Mak HY, Nelson LS, Basson M, Johnson CD, Ruvkun G. 2006. Polygenic control of Caenorhabditis
896 elegans fat storage. *Nat Genet* **38**: 363–368.

897 Martina JA, Chen Y, Gucek M, Puertollano R. 2012. MTORC1 functions as a transcriptional regulator of
898 autophagy by preventing nuclear transport of TFEB. *Autophagy* **8**: 903–914.

899 Meissner B, Boll M, Daniel H, Baumeister R. 2004. Deletion of the Intestinal Peptide Transporter Affects
900 Insulin and TOR Signaling in Caenorhabditis elegans. *J Biol Chem* **279**: 36739–36745.

901 Miesenböck G, De Angelis DA, Rothman JE. 1998. Visualizing secretion and synaptic transmission with
902 pH-sensitive green fluorescent proteins. *Nature* **394**: 192–195.

903 Minevich G, Park DS, Blankenberg D, Poole RJ, Hobert O. 2012. CloudMap: A Cloud-Based Pipeline for
904 Analysis of Mutant Genome Sequences. *Genetics* **192**: 1249–1269.

905 Nehrke K. 2003. A Reduction in Intestinal Cell pH Due to Loss of the Caenorhabditis elegans Na+/H+
906 Exchanger NHX-2 Increases Life Span. *J Biol Chem* **278**: 44657–44666.

907 Niemeyer MI, González-Nilo FD, Zúñiga L, González W, Cid LP, Sepúlveda FV. 2007. Neutralization of
908 a single arginine residue gates open a two-pore domain, alkali-activated K^+ channel. *Proc Natl*
909 *Acad Sci* **104**: 666–671.

910 Oishi A, Gengyo-Ando K, Mitani S, Mohri-Shiomi A, Kimura KD, Ishihara T, Katsura I. 2009. FLR-2,
911 the glycoprotein hormone alpha subunit, is involved in the neural control of intestinal functions in
912 *Caenorhabditis elegans*. *Genes Cells* **14**: 1141–1154.

913 O'Kelly I, Butler MH, Zilberberg N, Goldstein SAN. 2002. Forward transport. 14-3-3 binding overcomes
914 retention in endoplasmic reticulum by dibasic signals. *Cell* **111**: 577–588.

915 O'Rourke EJ, Ruvkun G. 2013. MXL-3 and HLH-30 transcriptionally link lipolysis and autophagy to
916 nutrient availability. *Nat Cell Biol* **15**: 668–676.

917 O'Rourke EJ, Soukas AA, Carr CE, Ruvkun G. 2009. C. elegans Major Fats Are Stored in Vesicles
918 Distinct from Lysosome-Related Organelles. *Cell Metab* **10**: 430–435.

919 Perez MF, Lehner B. 2019. Vitellogenins - Yolk Gene Function and Regulation in Caenorhabditis elegans.
920 *Front Physiol* **10**: 1067.

921 Peterson ND, Icso JD, Salisbury JE, Rodríguez T, Thompson PR, Pukkila-Worley R. 2022. Pathogen
922 infection and cholesterol deficiency activate the C. elegans p38 immune pathway through a TIR-
923 1/SARM1 phase transition. *eLife* **11**: e74206.

924 Pfeiffer J, Johnson D, Nehrke K. 2008. Oscillatory Transepithelial H+ Flux Regulates a Rhythmic
925 Behavior in C. elegans. *Curr Biol* **18**: 297–302.

926 Raizen DM, Lee RY, Avery L. 1995. Interacting genes required for pharyngeal excitation by motor neuron
927 MC in Caenorhabditis elegans. *Genetics* **141**: 1365–1382.

928 Ramalho JJ, Sepers JJ, Nicolle O, Schmidt R, Cravo J, Michaux G, Boxem M. 2020. C-terminal
929 phosphorylation modulates ERM-1 localization and dynamics to control cortical actin organization
930 and support lumen formation during *C. elegans* development. *Development* dev.188011.

931 Reyes R, Duprat F, Lesage F, Fink M, Salinas M, Farman N, Lazdunski M. 1998. Cloning and Expression
932 of a Novel pH-sensitive Two Pore Domain K+ Channel from Human Kidney. *J Biol Chem* **273**:
933 30863–30869.

934 Roczniak-Ferguson A, Petit CS, Froehlich F, Qian S, Ky J, Angarola B, Walther TC, Ferguson SM. 2012.
935 The transcription factor TFEB links mTORC1 signaling to transcriptional control of lysosome
936 homeostasis. *Sci Signal* **5**: ra42.

937 Rödström KEJ, Kiper AK, Zhang W, Rinné S, Pike ACW, Goldstein M, Conrad LJ, Delbeck M, Hahn
938 MG, Meier H, et al. 2020. A lower X-gate in TASK channels traps inhibitors within the vestibule.
939 *Nature* **582**: 443–447.

940 Schindelin J, Arganda-Carreras I, Frise E, Kaynig V, Longair M, Pietzsch T, Preibisch S, Rueden C,
941 Saalfeld S, Schmid B, et al. 2012. Fiji: an open-source platform for biological-image analysis. *Nat*
942 *Methods* **9**: 676–682.

943 Schroeder DF, McGhee JD. 1998. Anterior-posterior patterning within the *Caenorhabditis elegans*
944 endoderm. *Development* **125**: 4877–4887.

945 Seah NE, de Magalhaes Filho CD, Petrashen AP, Henderson HR, Laguer J, Gonzalez J, Dillin A, Hansen
946 M, Lapierre LR. 2016. Autophagy-mediated longevity is modulated by lipoprotein biogenesis.
947 *Autophagy* **12**: 261–272.

948 Settembre C, De Cegli R, Mansueto G, Saha PK, Vetrini F, Visvikis O, Huynh T, Carissimo A, Palmer D,
949 Klisch TJ, et al. 2013. TFEB controls cellular lipid metabolism through a starvation-induced
950 autoregulatory loop. *Nat Cell Biol* **15**: 647–658.

951 Settembre C, Di Malta C, Polito VA, Garcia Arencibia M, Vetrini F, Erdin S, Erdin SU, Huynh T, Medina
952 D, Colella P, et al. 2011. TFEB links autophagy to lysosomal biogenesis. *Science* **332**: 1429–1433.

953 Sheng M, Hosseinzadeh A, Muralidharan SV, Gaur R, Selstam E, Tuck S. 2015. Aberrant Fat Metabolism
954 in Caenorhabditis elegans Mutants with Defects in the Defecation Motor Program ed. A.C. Hart.
955 *PLOS ONE* **10**: e0124515.

956 Singh J, Aballay A. 2019. Microbial Colonization Activates an Immune Fight-and-Flight Response via
957 Neuroendocrine Signaling. *Dev Cell* **49**: 89-99.e4.

958 Singh R, Kaushik S, Wang Y, Xiang Y, Novak I, Komatsu M, Tanaka K, Cuervo AM, Czaja MJ. 2009.
959 Autophagy regulates lipid metabolism. *Nature* **458**: 1131–1135.

960 Spanier B, Lasch K, Marsch S, Benner J, Liao W, Hu H, Kienberger H, Eisenreich W, Daniel H. 2009.
961 How the Intestinal Peptide Transporter PEPT-1 Contributes to an Obesity Phenotype in
962 Caenorhabditits elegans ed. I.A. Hansen. *PLoS ONE* **4**: e6279.

963 Sparta B, Kosaisawe N, Pargett M, Patankar M, DeCuzzi N, Albeck JG. 2023. Continuous sensing of
964 nutrients and growth factors by the mTORC1-TFEB axis eds. I. Topisirovic, D.E. James, and I.
965 Topisirovic. *eLife* **12**: e74903.

966 Sulston JE, Schierenberg E, White JG, Thomson JN. 1983. The embryonic cell lineage of the nematode
967 Caenorhabditis elegans. *Dev Biol* **100**: 64–119.

968 Suzuki Y, Kikuchi K, Numayama-Tsuruta K, Ishikawa T. 2022. Reciprocating intestinal flows enhance
969 glucose uptake in C. elegans. *Sci Rep* **12**: 15310.

970 Take-uchi M, Kawakami M, Ishihara T, Amano T, Kondo K, Katsura I. 1998. An ion channel of the
971 degenerin/epithelial sodium channel superfamily controls the defecation rhythm in *Caenorhabditis*
972 *elegans*. *Proc Natl Acad Sci* **95**: 11775–11780.

973 Take-uchi M, Kobayashi Y, Kimura KD, Ishihara T, Katsura I. 2005. FLR-4, a Novel Serine/Threonine
974 Protein Kinase, Regulates Defecation Rhythm in *Caenorhabditis elegans*. *Mol Biol Cell* **16**: 1355–
975 1365.

976 Talley EM, Solorzano G, Lei Q, Kim D, Bayliss DA. 2001. Cns distribution of members of the two-pore-
977 domain (KCNK) potassium channel family. *J Neurosci Off J Soc Neurosci* **21**: 7491–7505.

978 Tan KT, Luo S-C, Ho W-Z, Lee Y-H. 2011. Insulin/IGF-1 receptor signaling enhances biosynthetic
979 activity and fat mobilization in the initial phase of starvation in adult male C. elegans. *Cell Metab*
980 **14**: 390–402.

981 Thomas JH. 1990. Genetic analysis of defecation in Caenorhabditis elegans. *Genetics* **124**: 855–872.

982 Thwaites DT, Kennedy DJ, Raldua D, Anderson CMH, Mendoza ME, Bladen CL, Simmons NL. 2002.
983 H+/dipeptide absorption across the human intestinal epithelium is controlled indirectly via a
984 functional Na+/H+ exchanger. *Gastroenterology* **122**: 1322–1333.

985 Torzone SK, Park AY, Breen PC, Cohen NR, Dowen RH. 2023. Opposing action of the FLR-2
986 glycoprotein hormone and DRL-1/FLR-4 MAP kinases balance p38-mediated growth and lipid
987 homeostasis in C. elegans ed. A.P. Gould. *PLOS Biol* **21**: e3002320.

988 Trapp S, Isabel Aller M, Wisden W, Gourine AV. 2008. A Role for TASK-1 (KCNK3) Channels in the
989 Chemosensory Control of Breathing. *J Neurosci* **28**: 8844–8850.

990 Tsirigos KD, Peters C, Shu N, Käll L, Elofsson A. 2015. The TOPCONS web server for consensus
991 prediction of membrane protein topology and signal peptides. *Nucleic Acids Res* **43**: W401-407.

992 Verma S, Jagtap U, Goyala A, Mukhopadhyay A. 2018. A novel gene-diet pair modulates C. elegans aging
993 ed. S.S. Lee. *PLOS Genet* **14**: e1007608.

994 Wang H, Girskis K, Janssen T, Chan JP, Dasgupta K, Knowles JA, Schoofs L, Sieburth D. 2013.
995 Neuropeptide Secreted from a Pacemaker Activates Neurons to Control a Rhythmic Behavior.
996 *Curr Biol CB* **23**: 746–754.

997 Yue Z, Li Y, Yu B, Xu Y, Chen L, Chitturi J, Meng J, Hung W, Tian Y, Mouridi SE, et al. 2022. A Leak K^+
998 Channel TWK-40 Regulates Rhythmic Motor Program in *C. elegans*.
999 http://biorxiv.org/lookup/doi/10.1101/2022.04.09.487752 (Accessed April 18, 2024).

000 Zhang N, Khan LA, Membreno E, Jafari G, Yan S, Zhang H, Gobel V. 2017. The C. elegans Intestine As a
001 Model for Intercellular Lumen Morphogenesis and In Vivo Polarized Membrane Biogenesis at the
002 Single-cell Level: Labeling by Antibody Staining, RNAi Loss-of-function Analysis and Imaging. *J*
003 *Vis Exp JoVE* 56100.

004 Zhou C, Zhou Q, He X, He Y, Wang X, Zhu X, Zhang Y, Ma L. 2022. Differential modulation of C.
005 elegans motor behavior by NALCN and two-pore domain potassium channels ed. A.C. Hart.
006 *PLOS Genet* **18**: e1010126.

007

008 **FIGURES**

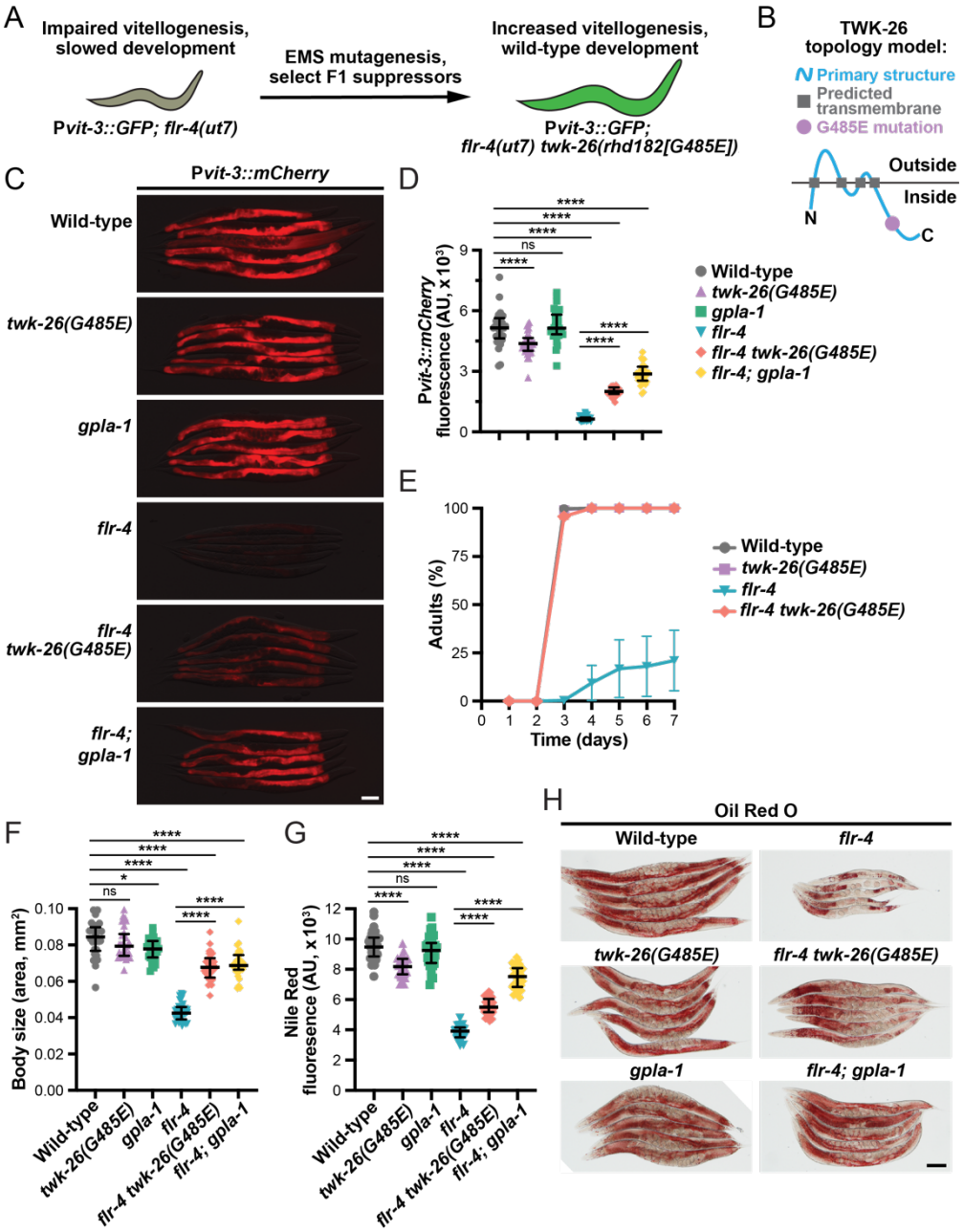

Figure 1. A *twk-26* mutation suppresses the growth and lipid metabolism defects exhibited by the *flr-4* mutant. (A) A diagram illustrating the design of an EMS mutagenesis screen using the *mgIs70[*P*vit-3::GFP]* vitellogenesis reporter. Mutations that suppressed the slow growth or the reporter expression defects of the *flr-4(ut7)* mutant were selected in the F1 generation, thereby enriching for gain-of-function mutations. (B) A transmembrane topology prediction of TWK-26 based on the amino acid sequence. The *twk-26(G485E)* mutation resides in the C-terminal tail. (C) Representative overlaid DIC and mCherry fluorescence images (scale bar, 100µm) and (D) quantification of P*vit-3::mCherry* expression (median and interquartile range; ns, not significant, ****, *P*<0.0001, one-way ANOVA) for the indicated strains at day 1 of adulthood. (E) Growth rate of the indicated strains (mean +/− SEM of 3 independent experiments). Data shown here are also displayed in Figure S1B. (F) Body size of the indicated strains at day 1 of adulthood (median and interquartile range; ns, not significant, *, *P*<0.05, ****, *P* <0.0001, one-way ANOVA). (G) Quantification of Nile Red staining of day 1 adults (median and interquartile range; ns, not significant, ****, *P*<0.0001, one-way ANOVA). (H) Representative images of the indicated strains stained with Oil Red O (day 1 adults; scale bar, 100µm). (C-H) All strains contain the *rhdSi42[*P*vit-3::mCherry]* reporter transgene.

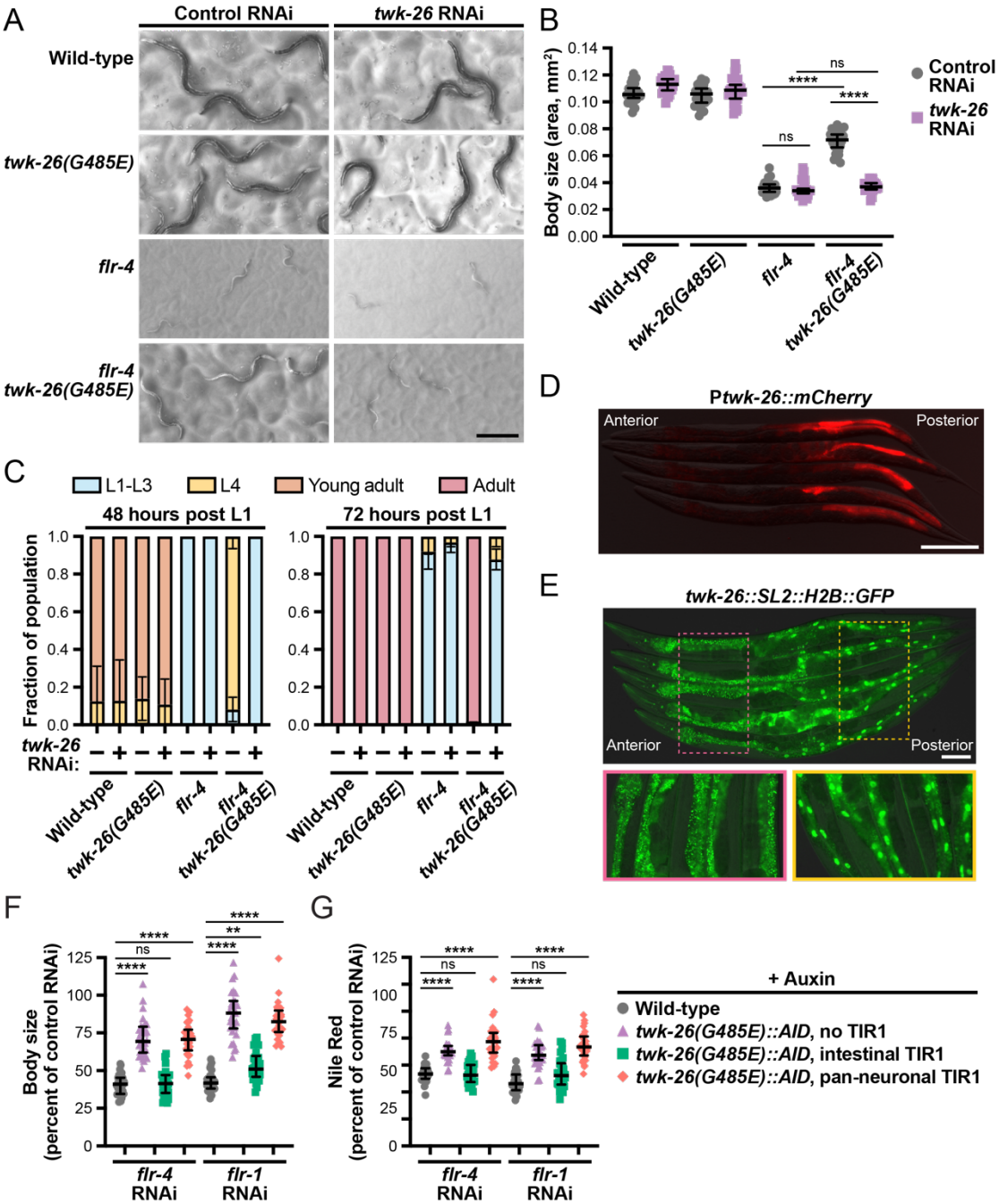

Figure 2. Activation of intestinal TWK-26 suppresses *flr-4* mutant defects. (A) Representative bright field images of the indicated strains subjected to control or *twk-26* RNAi for 72 hours (scale bar, 250µm). (B) Body size of the indicated strains (day 1 adults; median and interquartile range; ns, not significant, ****, *P*<0.0001, one-way ANOVA). (C) Fraction of the population at each developmental stage (mean +/- SD) after treatment of the indicated strains with control or *twk-26* RNAi for 48 or 72 hours. Representative overlaid DIC and fluorescence images of day 1 adult animals carrying (D) a high-copy P*twk-26::mCherry* transgene (scale bar, 200µm) or (E) a *twk-26::SL2::H2B::GFP* allele generated by CRISPR/Cas9 editing (scale bar, 100µm). Quantification of (F) body size or (G) Nile Red staining of the indicated strains subjected to *flr-4* or *flr-1* RNAi following intestinal (P*ges-1::TIR1*) or pan-neuronal (P*rgef-1::TIR1*) depletion of TWK-26::AID protein (4mM auxin) in day 1 adults. All data are normalized to empty vector RNAi controls and displayed as median and interquartile range (ns, not significant, **, *P*=0.0027, ****, *P*<0.0001, one-way ANOVA). (A-C, E, F) All strains contain the P*vit-3::mCherry* reporter.

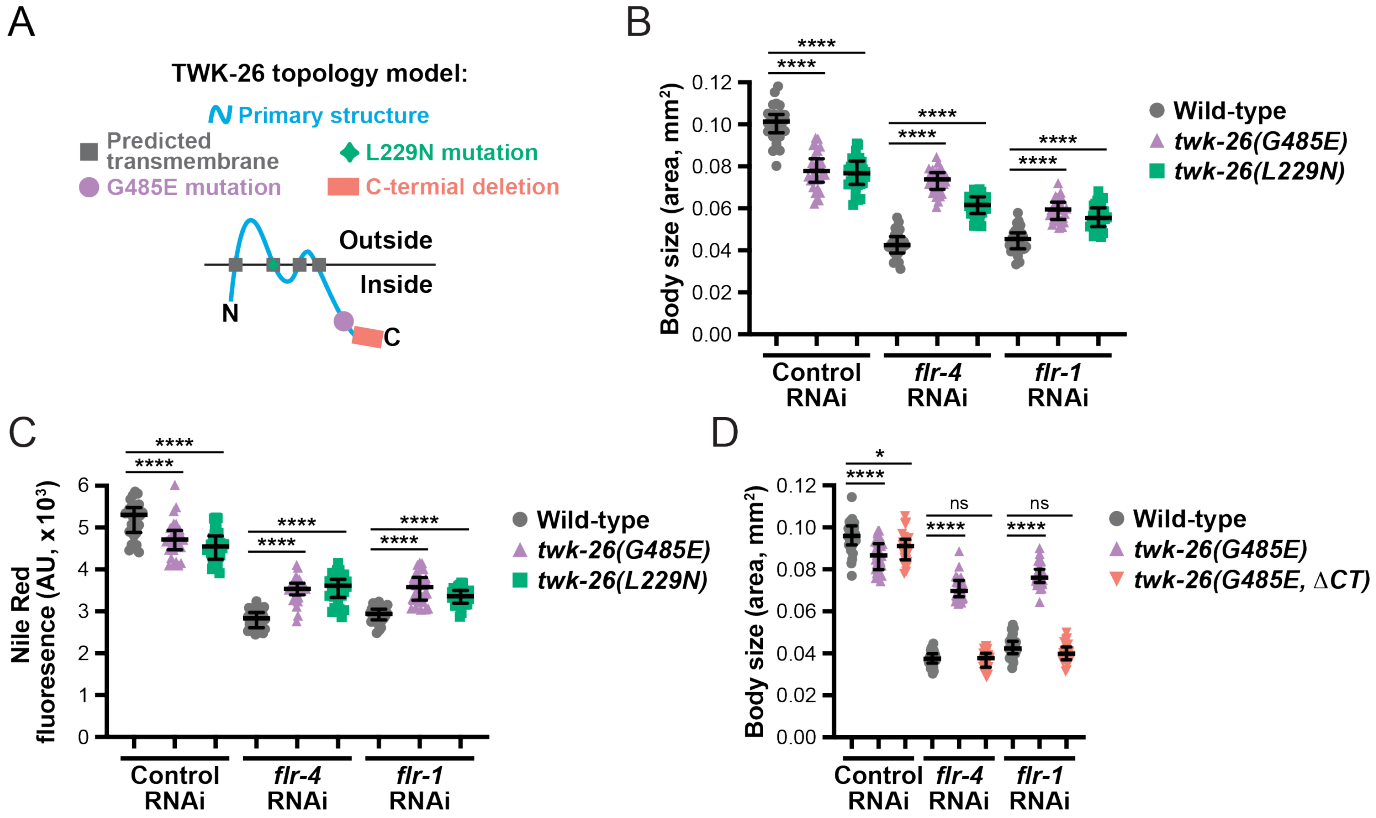

Figure 3. Increased TWK-26 channel gating suppresses the *flr-4* mutation. (A) A transmembrane topology prediction of TWK-26 based on amino acid sequence. The *twk-26(G485E)* mutation resides in the C-terminal tail while the *twk-26(L229N)* mutation is positioned in the second transmembrane domain. The *twk-26(G485E, ΔCT)* strain contains a frameshift at Thr502, resulting in loss of amino acids 503-519. Quantification of (B) body size and (C) Nile Red staining for the indicated strains subjected to control, *flr-4*, or *flr-1* RNAi (day 1 of adults; median with interquartile range; ****, $P<0.0001$, one-way ANOVA). (D) Body size measurements of day 1 adult wild-type or *twk-26* mutant animals carrying the *rhdSi42[*P*vit-3::mCherry]* transgene following control, *flr-4*, or *flr-1* RNAi (median with interquartile range; ns, not significant, *, $P=0.0136$, ****, $P<0.0001$, one-way ANOVA).

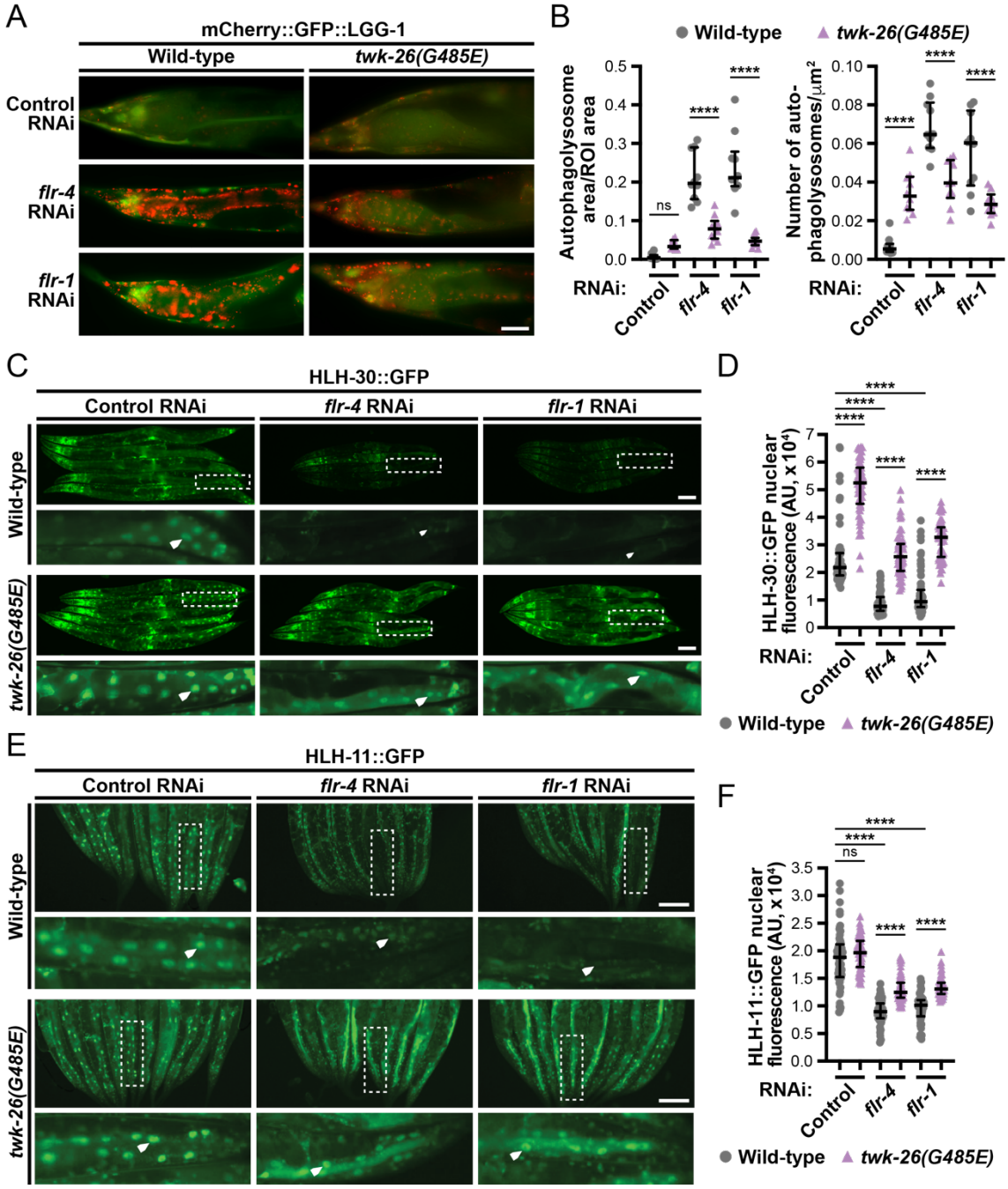

Figure 4. TWK-26 G485E limits autophagy in the *flr-4* and *flr-1* mutants. (A) Representative merged images of mCherry::GFP::LGG-1 puncta in posterior intestinal cells of wild-type or *twk-26(G485E)* day 1 adult animals subjected to control, *flr-4*, or *flr-1* RNAi (scale bar, 25μm). Autolysosomes are labelled by mCherry alone since the GFP signal is quenched. (B) Quantification of the area (left panel) and total number (right panel) of autolysosomes in the posterior intestine (median and interquartile range; ns, not significant, ***, P=0.0001, ****, P<0.0001, one-way ANOVA). (C) Representative HLH-30::GFP fluorescence images (white arrowheads indicate intestinal nuclei; scale bars, 100μm) and (D) quantification of nuclear HLH-30::GFP signal (median with interquartile range; ****, P<0.0001, one-way ANOVA) in wild-type or *twk-26(G485E)* day 1 adults subjected to control, *flr-4*, or *flr-1* RNAi. (E) Representative HLH-11::GFP fluorescence images (white arrowheads, intestinal nuclei; scale bars, 100μm) and (F) quantification of nuclear HLH-11::GFP signal (median with interquartile range; ns, not significant, ****, P<0.0001, one-way ANOVA) in wild-type or *twk-26(G485E)* day 1 adult animals following control, *flr-4*, or *flr-1* RNAi.

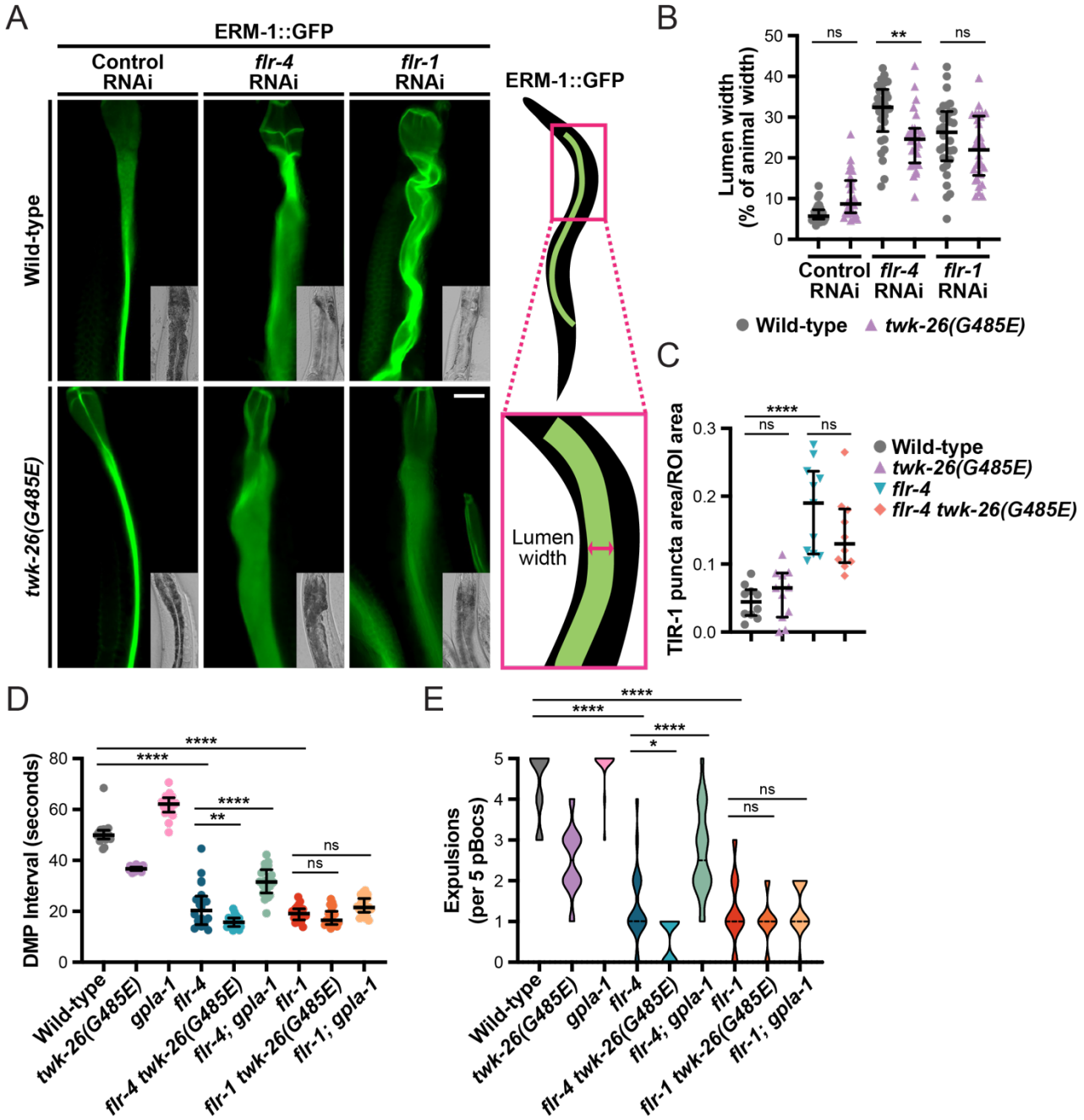

Figure 5. The TWK-26 G485E mutation fails to suppress the intestinal morphology and defecation defects of the *flr-4* and *flr-1* mutants. (A) Representative fluorescence images, as well as DIC insets, of ERM-1::GFP or ERM-1::GFP*; twk-26(G485E)* day 1 adult animals subjected to control, *flr-4*, or *flr-1* RNAi (scale bar, 25µm). The ERM-1::GFP protein marks the intestinal lumen. (B) Quantification of lumen width as a percentage of body width at the measurement site (median and interquartile range; ns, not significant, **, *P*=0.0039, ****, *P*<0.0001, one-way ANOVA). (C) Quantification of TIR-1::wrmScarlet puncta size in the posterior intestine of the indicated strains at day 1 of adulthood (median and interquartile range; ns, not significant, ****, *P*<0.0001, one-way ANOVA). (D) Measurements of the time between posterior body wall contractions (pBoc). Each data point represents the average DMP interval calculated across five pBoc events per individual (median and interquartile range; ns, not significant, **, *P*=0.0014, ****, *P*<0.0001, one-way ANOVA). (E) The number of pBoc events that were accompanied by intestinal expulsion (Exp) across the five observed DMP intervals. Distributions are shown as truncated violin plots with the median value indicated (dashed line). (D-E) Ten animals were scored for two independent experiments for a total of 20 animals per genotype (strains contain *rhdSi42*).

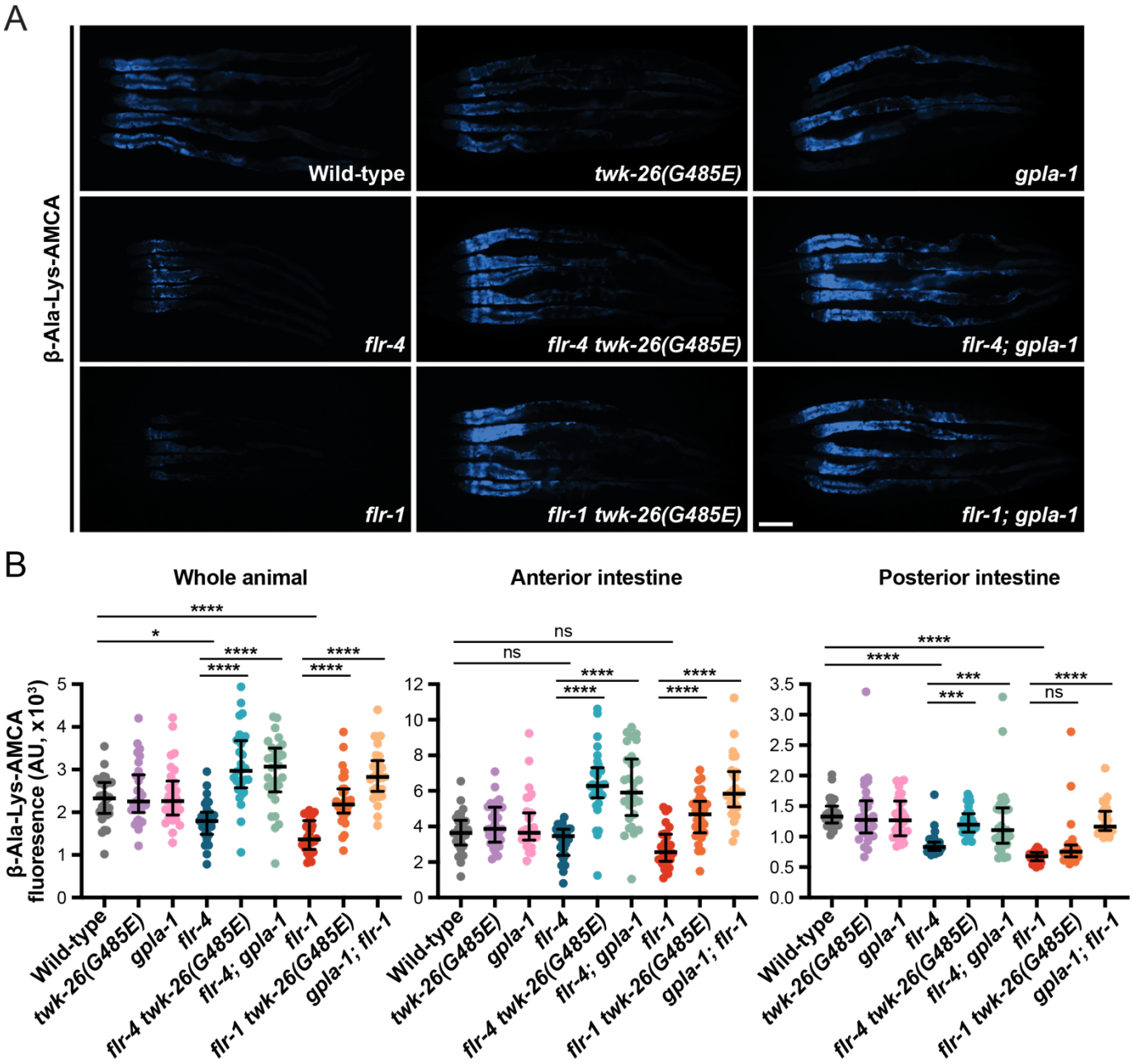

Figure 6. Activation of TWK-26 restores intestinal dipeptide absorption in the absence of *flr-4* and *flr-1*. (A) Representative fluorescence images of day 1 adult animals incubated for 3 hours in 1mM β-Ala-Lys-AMCA, a fluorescently labeled dipeptide (5 animals per image; scale bar, 100μm). Animals are oriented anterior (left) to posterior (right). (B) Quantification of the fluorescent signal in the whole animal or in specified regions of the intestine (anterior region, head to the vulva; posterior region, vulva to the tail). Data are presented as median and interquartile range (ns, not significant, *, P=0.012, **, P<0.01, ***, P<0.001, ****, P<0.0001, one-way ANOVA performed for the indicated comparisons).

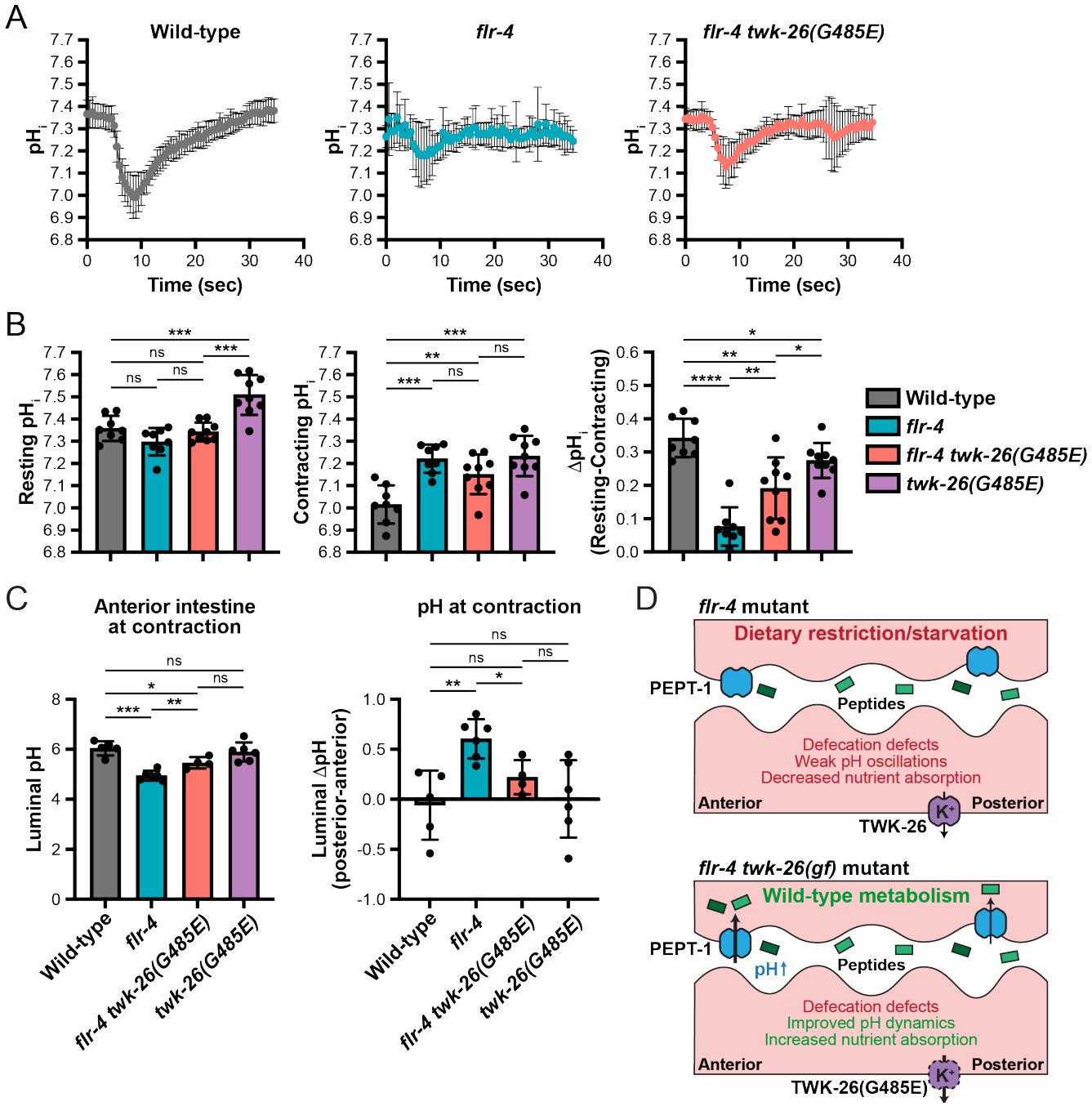

Figure 7. The *flr-4* mutant displays defects in intestinal pH oscillations which are rectified by TWK-26 G485E. (A) A time course (relative to pBoc) of the intracellular pH (pH_i) of wild-type (N=8), *flr-4(ut7)* (N=9), and *flr-4(ut7) twk-26(G485E)* (N=9) day 1 adult animals expressing the pHluorin transgene. Data are plotted as the mean and SD. (B) Mean resting pH_i (left panel) and contracting pH_i (middle panel) calculated using the Boltzmann calibration, as well as the ΔpH_i (right panel), for each of the indicated pHluorin strains (N=8-9 animals per genotype; mean +/- SD; ns, not significant, *, $P<0.05$, **, $P<0.01$, ***, $P<0.001$, ****, $P<0.0001$, Brown-Forsythe and Welch ANOVA followed by Fishers LSD Test). (C) Measurements of the anterior luminal pH at the time of intestinal contraction in animals fed dextran-conjugated Oregon Green 488 (left panel). The difference in luminal pH between the posterior and anterior intestine is also shown (right panel). All data are presented as mean and SD (N=4-7 animals per genotype; ns, not significant, *, $P<0.05$, **, $P<0.01$, ***, $P<0.001$, Brown-Forsythe and Welch ANOVA followed by Fishers LSD Test). (D) A model depicting how TWK-26 G485E may restore nutrient absorption and metabolic homeostasis upon loss of *flr-4*.